The International DORIS Service contribution to ITRF2020

Guilhem Moreaux[a,*], Frank G. Lemoine[b], Hugues Capdeville[a], Michiel Otten[c], Petr Štěpánek[d], Jérôme Saunier[e], Pascale Ferrage[f]

[a] *Collecte Localisation Satellites, 8-10 rue Hermès, Parc technologique du Canal, 31520 Ramonville Saint-Agne, France*
[b] *NASA, Goddard Space Flight Center, Code 698, Greenbelt, MD 20771, USA*
[c] *ESA/European Space Operation Center, Robert-Boch-Strasse 5, 64293 Darmstadt, Germany*
[d] *Geodetic Observatory Pecný, Research Institute of Geodesy, Topography and Cartography, Ondřejov 244, 25165, Czech Republic*
[e] *Institut National de l'information Géographique et forestière, 73 avenue de Paris, 94165 Saint Mandé, France*
[f] *Centre National d'Etudes Spatiales, 18 avenue Edouard Belin, 31401 Toulouse Cedex 9, France*

Abstract

For the realization of the 2020 International Terrestrial Reference Frame (ITRF2020), the International DORIS Service delivered to the International Earth Rotation and Reference Systems Service (IERS) a set of 1456 weekly solution files from 1993.0 to 2021.0 including station coordinates and Earth orientation parameters (EOPs). The data come from fourteen DORIS satellites: TOPEX/Poseidon, SPOT-2, SPOT-3, SPOT-4, SPOT-5, Envisat, Jason-1, Jason-2, Cryosat-2, Saral, HY-2A, Jason-3, Sentinel-3A and Sentinel-3B. In their processing, the four analysis centers which contributed to the DORIS combined solution used the latest time variable gravity models, the new mean pole and diurnal-subdiurnal tidal EOP models recommended by IERS. In addition, all the analysis centers included in their processing precise SPOT-5 solar panel angle values and quaternions for, at least, the Jason satellites. Furthermore, a new Alcatel phase center variation model was implemented for the ITRF2020 processing. The main objective of this study is to present the combination process and to analyze the impact of the new modeling on the performance of the new combined

*Corresponding author. Tel: +33 561 394 847
Email address: gmoreaux@groupcls.com (Guilhem Moreaux)

solution. Comparisons with the IDS contribution to ITRF2014 show that i) the application of the new phase center variations for the Alcatel DORIS ground antennas in the data processing combined with the gradual replacement over time of the Alcatel by Starec antennas implies a scale drift from 1993.0 to 2002.5 and ii) thanks to a better modeling of the surface forces on the satellites, the new combined solution shows smaller annual and 118-day signals in the geocenter. A new DORIS terrestrial reference frame was computed to evaluate the intrinsic quality of the new combined solution. That evaluation shows that over almost the full time span the intrinsic IDS scale values lie in a range of ±5 mm. After mid-2008, the new DORIS reference frame has an internal position consistency in North-East-Up better than 7.5 mm.

Keywords: DORIS, Intra-technique combination, Terrestrial Reference Frame, ITRF, Polar Motion

---

1. Introduction

Periodically, the International Earth Rotation and Reference Systems Service (IERS) initiates a call for participation to develop a new realization of the International Terrestrial Reference Frame (ITRF). Since 2005, the DORIS (Doppler Orbitography Radiopositioning Integrated by Satellite) technique has contributed to the realization of the ITRF as one of the four geodetic space techniques with Global Navigation Satellite Systems (GNSS), Very Long Baseline Interferometry (VLBI) and Satellite Laser Ranging (SLR). In preparation of the ITRF2008, the International DORIS Service (IDS, Willis et al., 2010) initialized an IDS Combination Center (CC) to combine DORIS solutions from all the IDS Analysis Centers (ACs) in order to deliver a single homogenized and improved DORIS solution to the IERS. Thus, the IDS contributed to the ITRF2008 (Valette et al., 2010) and ITRF2014 (Moreaux et al., 2016) by delivering weekly solution files including weekly DORIS station positions and daily X and Y pole coordinates from 1993.0 to 2009.0 and 2015.0, respectively.

In addition to the realization of the DORIS contribution to the ITRF, the IDS CC routinely (on a quarterly basis with a latency of three months) evaluates and combines single AC solutions. Then, the weekly combined solution files, as well as the updated DORIS station coordinate time series and the X and Y pole coordinate time series, are delivered to the IDS Data Centers (CDDIS and IGN, see Noll and Soudarin, 2006). As a byproduct of the combined solution files, the IDS CC regularly updates the DPOD (DORIS

terrestrial reference frame for Precise Orbit Determination, see Moreaux et al., 2019) solution which includes mean positions and velocities of all the DORIS stations. The DPOD solutions, which are cumulative solutions of the up-to-date (in time and number of stations) IDS combined series aligned to the current ITRF, are designed to support the computation of precise orbits of the altimetry missions such as TOPEX/Poseidon, Envisat, Jason-1, Jason-2, Cryosat-2, HY-2A, Saral/AltiKa, Jason-3 and Sentinel-3A.
Since the delivery to the IERS of the IDS contribution to the ITRF2014 in 2015, the ground and space components of the DORIS system have continued to evolve. In parallel to the routine activities of maintaining the operation of the legacy DORIS sites, the CNES and the IGN have continued to find new sites that attempt to fill the gaps in tracking coverage of the DORIS ground network. Thus, new beacons were installed, for example, in Managua (Nicaragua), Mangilao (Guam Island, USA) and San Juan (Argentina). In addition, in the context of the Global Geodetic Observing System (GGOS) of the International Association of Geodesy project and the need to develop more multi-technique sites, the IDS has installed new stations in Wettzell (Germany - four techniques) and relocated its legacy station in Ny-Ålesund (Svalbard, Norway), which was some kilometers away from the new four-technique site. In order to extend the DORIS system beyond to 2030, a new generation of DORIS beacons has been developed and, in mid-2019, the first model was installed at St-John's (Canada). In addition, a consolidated version of the Starec ground antennas has started to be deployed. On the DORIS constellation side, since the end of the SPOT-5 mission late 2015, all the satellites of the DORIS constellation carry the latest (third) generation of receivers, that allow the tracking of up to seven DORIS stations simultaneously. For comparison, the first (resp. second) generation of DORIS receivers could only track up to one (resp. two) beacons at one time. As discussed by Auriol and Tourain (2010), the third generation of DORIS receivers led to a significant increase of observations especially at lower elevations. In terms of DORIS data processing, in addition to the implementation of the latest IERS standards (mean pole model, diurnal-subdiurnal tidal EOP model,...), the IDS ACs updated their time-variable geopotential and ocean tide models (see Table A.11). Moreover, following the IDS ITRF2020 requirements, the new DORIS series implemented a new version of the Alcatel ground antenna phase variation model, introduced corrected SPOT-5 solar array pitch angles and used quaternions for the attitude modeling of Jason (for the spacecraft body and the solar arrays) and Cryosat-2 satellites. Furthermore, with the extension of the use of the new DORIS data format (RINEX - for all the missions with onboard third gen-

eration of DORIS receiver Lemoine et al., 2016), the IDS ACs consolidated their own data processing and applied elevation-dependent down-weighting of DORIS data.
This paper deals with the elaboration and validation/evaluation of the IDS contribution to the ITRF2020. The paper is organized as follows: in section 2, we briefly review the major new modelling introduced for the ITRF2020 processing while section 3 summarizes the combination processing strategy. Then, section 4 introduces the IDS contribution to the ITRF2020. In section 5, we analyze the DORIS contribution to ITRF2020 with respect to the ITRF2014 (Altamimi et al., 2016) solution in terms of (1) translation and scale parameters; (2) station positions and week-to-week repeatability; (3) EOPs. Comparisons with the previous IDS contribution to ITRF2014 demonstrate the impacts of all the improvements (satellites and stations technical upgrades as well as in the DORIS data processing). Section 6 summarizes the internal performance of the IDS ITRF2020 contribution with respect to its position and velocity cumulative solution. Finally, we provide new perspectives and discuss future challenges for the IDS CC (section 7).

2. IDS Combination Input

This section addresses the major evolutions in the DORIS modeling since the release of the ITRF2014.
In the context of the preparation for ITRF2020, the IDS CC received time series contributions from the four operational IDS ACs (see Table 1). From Table 1, we see that each AC uses a distinct software package for orbit determination. The diversity of the software packages helps to detect any peculiarity or anomaly in the data processing and helps to ensure that a reliable IDS combination can be provided.
As with the IDS processing for ITRF2014, the data prior to 1993 were not used because i) the DORIS station network was not fully in place and operational until the beginning of the TOPEX/Poseidon mission in August 1992 (Fagard, 2006); ii) only a limited amount of DORIS data were publicly available before 1993.0; and iii) the level of precision of the single-satellite solutions of the first DORIS missions is not compatible with what is expected for geodetic positioning (Willis, 2007). The requirement for the ITRF2020 is that the time span should include the last days of 2020. Thus, as summarized in Table 2, each AC delivered approximately 1460 weekly solution files

in SINEX (Software INdependent EXchange) format[1] from 1993.0 to 2021.0 including station positions and daily EOPs (Earth Orientation Parameters). Whereas ESA and GSC provided SINEX files in NEQ (Normal EQuations) format, GOP and GRG adopted the variance-covariance format.
Given the IDS ITRF2020 time span (1993.0 to 2021.0), the DORIS core constellation included the Cryosat-2, Envisat, HY-2A, Jason-2&3, Saral, Sentinel-3A, SPOT-2 to SPOT-5 and the TOPEX/Poseidon missions (see Figure 1). The DORIS satellites HY-2C (launched on 2020/09/21) and Sentinel-6A (launched on 2020/11/21) arrived too late to be included for ITRF2020. In addition, the use of data from Jason-1, Sentinel-3B was considered optional and left to the choice of the individual ACs. Jason-1 was included by three ACs (ESA, GRG and GSC) and Sentinel-3B was processed by three ACs (ESA, GOP, GRG) - see Table 3 for more details).

2.1. New Alcatel Antenna Phase Center Variations

Starting from a plausible offset between Starec and Alcatel as revealed by Willis et al. (2007), the CNES initiated a radio-frequency characterization of these two types of antennas and released a Starec Phase Center Variation (PCV) model based on an anechoic chamber calibration. Unlike the Starec antenna, the Alcatel PCV model adopted for the ITRF2014 was inferred from the manufacturer specifications (Tourain et al., 2016). Then, for the ITRF2020 processing, CNES provided a new Alcatel PCV based on calibrations in an anechoic chamber (cf. Figure 2). Once the new model showed smaller DORIS data residuals (Štěpánek and Filler, 2022), the new model was recommended as a new IDS standard.

2.2. SAA Mitigation Strategies

As pointed out by Willis et al. (2004), the anomaly in Earth's magnetic field localized in and near South America and known as SAA (South Atlantic Anomaly) can alter the frequency behavior of some of the DORIS Ultrastable Oscillators (USOs) in the onboard receivers and may cause non-geophysical variations of the coordinates of the DORIS stations located in and near South America (e.g., Arequipa, Ascension, Cachoiera, Kourou, Le Lamentin...). The SAA effect depends on parameters such as the altitude of the satellite, the degree to which the USO was pre-irradiated prior to launch, the characteristics of the USO selected for flight, and the time the mission

[1] `http://www.iers.org/SharedDocs/Publikationen/EN/IERS/Documents/ac/sinex/sinex_v202_pdf`

(hence the USO) has spent on orbit. To overcome the SAA effect, the IDS suggested several mitigation strategies going from the development of a DORIS data correction model (see Lemoine and Capdeville (2006) for Jason-1, Belli et al. (2021) for Jason-2 and Capdeville et al. (2016) for SPOT-5) to the reduction of the SAA stations at the single-satellite solution level so they do not contribute to the estimation of the positions of these stations in the multi-satellite solution. The differences of the impact of the SAA-sensitive missions to the IDS AC multi-satellite solutions are the results of differences in both the single-satellite solution patterns (due to the diversity in the data processing) and the combination of these single-satellite solutions. Similarly to the ITRF2014 processing, for the realization of the DORIS contribution to the ITRF2020, the IDS recommended that Jason-1 be only only if the SAA-corrected data from Lemoine and Capdeville (2006) were used. In addition, the data from the mission should be added only from the end of TOPEX/Poseidon to the start of the Jason-2 missions (November 2004 to July 2008). That recommendation was made after observing that the addition of data from an alternate inclination compared to the near-polar orbits of the other DORIS satellites i) improved the ground station observation geometry, ii) improved the stability of the geocenter Z-translation and iii) reduced the X and Y pole estimates differences with IERS C04 series (see Moreaux et al., 2016). As with the ITRF2014 processing, the IDS also encouraged the ACs to use the SPOT-5 SAA data correction model by Capdeville et al. (2016) from 2005/12/27 (2005:261 - SPOT-5 cycle 138). Once Willis et al. (2016) revealed out a possible sensitivity of the Jason-2 Ulta Stable Oscillator (USO) to the SAA, the IDS initiated several studies which confirmed that Jason-2 was also impacted by the SAA, albeit at a much lower level than with Jason-1. Then, due to the lack of a Jason-2 data correction model at the start of the ITRF2020 reprocessing, the IDS suggested to reduce the SAA stations while performing the Jason-2 solution so the Jason-2 SAA sensitivity would not impact the multi-satellite solutions. The same strategy was also recommended for the Sentinel-3A&B missions after Jalabert and Mercier (2018) and Štěpánek et al (2020) showed the sensitivity of these missions to the SAA. On Sentinel-3A&B, the GPS and DORIS receivers use the same frequency reference (provided by the DORIS USO) so it is possible to observe the DORIS oscillator from the GPS measurements. Then, Jalabert and Mercier (2018) and Štěpánek et al (2020) demonstrated the impact of the SAA on the Sentinel-3A missions by using either GPS or DORIS only data for the estimation of the onboard frequency while processing the DORIS data for DORIS POD or positioning. This interesting method of improving the DORIS clock modelling for the Sentinel-

3A&B satellites was not validated in time to be used by DORIS ACs for ITRF2020, but we look forward to the application of this improved clock modeling in future work.
Making use of single-satellite SINEX solutions prepared as part of the ITRF2020 processing, we compared station positions from Jason-3 and HY-2A satellite-only solutions, since the HY-2A mission has not been identified as being sensitive to the SAA. These comparisons showed larger differences in the SAA region so, the IDS also suggested to apply the Jason-2-like SAA mitigation strategy also to the Jason-3 mission.

3. IDS Combined Solution

The construction of the IDS weekly combined solution for contribution to the ITRF2020 was performed in three steps: 1) evaluation/preprocessing of individual solutions from all the IDS ACs , 2) combination of the weekly solution files as output of step 1 and, 3) validation of the combined solution. The software package used for the IDS combination is the IGN CATREF (Combination and Analysis of Terrestrial Reference Frames) package (Altamimi et al., 2002a, - Section 3). The output of the IDS combination software are SINEX files containing station positions and EOPs in variance-covariance format. More details on the combination equations are given in Appendix C.
The construction of the IDS contribution to the ITRF2020 begins with the evaluation of all of the weekly solutions from the four IDS ACs. As a preliminary step, we convert solutions given in NEQ (Normal EQuations, as provided by ESA and GSC) format into solutions in variance-covariance (COV) format (see Appendix B). Then, we check for consistency between the DORIS station name acronyms and the DOMES numbers and we reject stations belonging to time periods when the data were identified as corrupt or invalid. That can be the consequence of, for example, antenna tilt due to corrosion or hurricanes, problems with either the cesium or maser clock or internal USO, failure of the beacon software, damage of the connecting cables... Afterwards, minimum constraints (cf. Section A.4 of Altamimi et al., 2002b) were applied to the loosely constrained AC solutions. Then, for each week and for each AC, stations with a posteriori position error in at least one component differing from the median value by more than 3.5 sigma were deleted from the solution. That test was set to reject stations that were poorly estimated. For each AC and each component, the median and sigma values were adjusted over eight time periods associated with the time evolution of the DORIS constellation. Furthermore, any AC weekly

solution with less than 20 stations after adding minimum constraints was rejected. Later, for each AC, we rejected weekly solutions corresponding to scale or translation parameters with respect to DPOD2014v51 (Moreaux et al., 2019) which differed from the corresponding median value by more than 5 sigma. Finally, for each AC and each week, we reject stations with position residuals with respect to the intrinsic position and velocity cumulative solution from 1993.0 to 2021.0 larger than 100 mm (in order to reject positions which look like outliers in the coordinate time series) and we delete weekly solutions with less than 20 stations satisfying the previous criteria. That latest test is a major evolution of the preprocessing compared to what was used for the ITRF2014 realization.

After all the weekly solutions from the IDS AC contributions have been successfully evaluated, the combination process can start. To strengthen the quality of the combined weekly solutions, we only computed solutions for weeks where we had contributions from at least two of four ACs. In addition, each week, we only estimated positions of stations which had been estimated by at least two ACs. The combination process is an iterative process with at most five iterations.

At each iteration, we reject from any contribution stations which display in at least one direction either larger residuals with the combined solution or larger normalized residuals (ratio between residual and sigma). By larger, we mean values which differ to the median value (over all the contributions and all the stations) by more than 3.5 times the standard deviation of the residuals. If, after rejecting the stations, a weekly contribution has less than 20 remaining stations then, the contribution is rejected for that week. A successive iteration is activated if the variance of unit weight is decreasing and differs from one by no more than 0.01 (1 percent). If not, the weekly combined solution as output of the iteration associated with the variance of unit weight closer to one is taken as the IDS combined solution.

Before delivering the new IDS combined solution to the IERS and the IDS Data Centers, the IDS CC proceeds to an internal validation similar to the one used for the evaluation of the IDS AC weekly solutions.

4. The IDS contribution to the ITRF2020

From the latest ESA, GOP, GRG and GSC multi-satellite solutions, the IDS 16 combined series was created by the IDS CC. To reduce the scale impact of adding Jason-2 (first satellite with DGXX DORIS receiver) mid-2008, GRG and GSC did not contribute to the combined scale between the end of TOPEX/Poseidon (late 2004) and the start of HY-2A (early 2011).

GRG and GSC scales display a V-shape pattern around the starting period of Jason-2 (see Figure 3). That feature results from i) a lower scale for the Jason-2 single-satellite solution while compared to the other AC single-satellite solutions and ii) a higher weighting for that mission while performing the AC multi-satellite solution. Since ESA and GOP solutions do not include any SAA mitigation strategy for Jason-3 and Sentinel3-A/B missions, in order to minimize the impact of these solutions on the coordinate time series of the SAA stations in the IDS combined solution, the contributions of ESA and GOP solutions to the IDS combined solutions were down-weighted after the addition of Jason-3 (2016:045.) Analysis of differences of EOPs of the individual series with respect to the IERS C04 series (Bizouard et al., 2019) showed that ESA series gave both larger differences and standard deviations compared to the performance of the three other IDS contributors. As a consequence, the ESA contribution was not included in the estimation of the combined pole.

Figure 4 shows the weekly variance factors (obtained by the so-called "degree of freedom estimation" method from Sillard, 1999) of each individual IDS AC contribution. The time series can be divided in three time periods with breaks in mid-2002 (inclusion of the first missions with onboard the second generation of DORIS receivers) and in early 2016 (inclusion of the Jason-3 and Sentinel-3A missions). Whereas the ESA, GOP, GRG and GSC variance factor time series look almost stable and indistinguishable over the first time period, we can divide the time series into two groups (ESA-GOP vs GRG-GSC) for the second time period depending on the slope. Furthermore, ESA, GOP and GRG time series exhibit an increase in late 2001 when the solar activity reaches its maximum intensity. GSC looks free of that pattern after reducing its arc length from 7 to 3.5 days or less from 1999 to 2003, and applying a reduced-dynamic orbit determination strategy. Since ESA and GOP did not implement any SAA mitigation strategy for Sentinel-3A, in order to minimize the impact of these two contributions on the coordinate time series of the DORIS stations located in and nearby South America (e.g., Arequipa, Cachoeira, Kourou, Le Lamentin...), the IDS CC deweighted by a factor of two these two contributions early 2016.

The new IDS combined solutions contains 1456 files over the 1461 expected ones (from 1993.0 to 2021.0). The five missing weeks were not delivered either due to too few stations in the combined solution (e.g., 1997:152) or, too few remaining stations in the AC contributions (e.g., 1998:102) or, for bad data quality (e.g., 1995:337) or, to poor positioning quality (e.g., 1994:009, 1995:344). Table 4 summarizes the contribution of each AC to the IDS 16 combined solutions and Figure 3 displays scale and translation of the AC

solutions with respect to the ITRF2014. More details on the IDS AC contributions to the ITRF2020 can be found in Capdeville et al. (submitted), Štěpánek at al. (submitted).
The combination process yields an IDS-ITRF2020 network (see Figure 5) of 201 stations located at 87 sites with 48 (resp. 39) sites located in the northern (resp. southern) hemisphere and with 43 (resp. 44) in the eastern (resp. western) hemisphere. For reference, the IDS network for the ITRF2014 included 160 stations located at 71 sites with 38 (resp. 33) sites in the northern (resp. southern) hemisphere and 36 (resp. 35) sites in the eastern (resp. western) hemisphere. The sixteen new sites include both old sites with less than 2.5 years of observations which were rejected at the early stage of the IDS processing for the ITRF2014 (Ajaccio, Flores, Huanine, Iquique, Le Lamentin, Lifou, Ottawa, Owenga, Paramushir, Santa-Maria, Tana) and totally new sites, i.e. installed since 2015: Managua (Nicaragua - 2016), Mangilao (Guam Island, U.S.A - 2018), Ny-Ålesund II (Svalbard, Norway - 2018), San Juan (Argentina - 2018), Wettzell (Germany - 2016). The addition of the old sites explains the slight lowering of the north-south distribution of the ITRF2020 network since most of these sites are in the northern hemisphere. Nevertheless, the DORIS ground network still displays a good north-south and east-west distribution. The IDS requirements for the installation of a DORIS station emphasizes the co-location with the three other space geodetic techniques (Saunier, submitted). Thus, 57 (resp. 13, 10) over the 87 DORIS sites host GNSS (resp. SLR, VLBI) stations. Furthermore, the four space geodetic techniques are present at 4 DORIS sites (Badary, Greenbelt, Yarragadee and Wettzell). In addition since the origin of the DORIS project, the DORIS technique is carried aboard CNES, NASA and ESA altimeter satellites, and has 35 ground colocations with tide gauges.
As shown by Figure 6, half of the DORIS sites have weekly position estimations for more than 787 weeks (nearly 15 years) with a maximum of 1451 weeks (nearly 28 years). Note that 26 sites (around 30%) have position estimations for more than 20 years, i.e. have been almost continuously operational since the beginning of the DORIS system. The five sites with the longest coordinate time series include Toulouse (France), Kauai (Hawaii, U.S.A.), Yarragadee (Australia), Libreville (Gabon), and Rio Grande (Argentina). The list of the five DORIS sites with the longest time series is unchanged since the IDS contribution to the ITRF2014. From that plot, we also observe that the coordinate time series of some sites were not extended since the realization of the ITRF2014. That does necessarily mean that the site was closed, it can be due to the delay in the renewal of radio frequency

transmission licenses or to the relocation of the DORIS station. Furthermore, in terms of observation time gap, the mean (resp. median) value over the 87 DORIS sites is of 61 (resp. 14) days. As these statistics refer to the sites, part of the gaps can be due to the delay between decommissioning a station and installing a new one. These small values emphasize the high level of efficiency of the DORIS network monitoring performed by IGN and CNES in cooperation with the local host agencies.

5. External evaluation of the IDS contribution to the ITRF2020

This section deals with the evaluation of the performance of the IDS contribution to the ITRF2020 with respect to the external reference: ITRF2014 (Altamimi et al., 2016). To see the improvements in the DORIS data processing achieved by the IDS ACs and the IDS CC since their contribution to the ITRF2014, in addition to the IDS 16 series, we evaluate the IDS contribution to the ITF2014: the IDS 09 series. Afterwards in that section, the Helmert parameter time series correspond to the alignment (by minimal contraints on the scale, translations and rotations) of each weekly IDS SINEX files with respect to the ITRF2014.

5.1. Scales

When comparing the IDS 09 and IDS 16 scales with respect to the ITRF2014 (see Figure 7), we found a different behavior between 1993.0 and mid-2002. Whereas the IDS 09 scale is almost flat, the IDS 16 scale depicts a negative linear trend of about -0.721 mm/yr. We speculate that the IDS 16 scale slope results from i) the use of two different Alcatel PCV models (section 2.1) for the ITRF2020 and for the ITRF2014 and, ii) the gradual replacement over time of the Alcatel by Starec ground antennas. To assess the impact of the DORIS ground antenna network, we did the following test (see Figure 8): we computed the IDS 16 scale with respect to the ITRF2014 with a pure Alcatel and a pure Starec network and, from the two mean scale values (15.85 mm for Alcatel vs 9.12 mm for Starec) we estimated a synthetic scale taking into account the time evolution of the percentage of Alcatel antennas on the DORIS network. Note that until almost the end of 2005, the DORIS network had simultaneously Alcatel and Starec antennas. Then, the very good agreement between the IDS 16 and synthetic scales supports our explanation of the IDS 16 scale drift between 1993.0 and mid-2002. As a result of the exclusion of SPOT-5 from the scales of the multi-satellite solutions from ESA, GRG and GSC, the IDS 16 scale looks more stable than the IDS 09 scale over the SPOT-5 time period. The IDS CC proposed to not include the

SPOT-5 scale due to its unexplained sawtoooth pattern showed by Moreaux et al. (2016). From Figure 7, we can also observe that the IDS 16 scale is less sensitive than the IDS 09 scale due to the addition mid-2008 of Jason-2 (first mission with a DORIS DGXX receiver onboard). This improvement in the IDS scale stability between ITRF2014 and ITRF2020 results from a lower impact of adding Jason-2 on the scale of half the IDS AC contributors (ESA and GOP - see Figure 3).

During the evaluation of the IDS contribution to the ITRF2014, Moreaux et al. (2016) pointed out a scale increase with respect to the ITRF2008 of about 10 mm late 2011 (2011:275, i.e. 2011/10/02). At that time, that scale increase was attributed to a scale jump for both Jason-2 and Cryosat-2 single-satellite solutions and to the addition of HY-2A which displayed a scale offset of $10 - 15$ mm. From Figure 7, we see that the IDS 09 still presents a scale increase with respect to the ITRF2014 in late 2011 whereas we do not observe such a phenomenon on the IDS 16 scale. This is explained by the fact that i) the scales of the Cryosat-2 and Jason-2 single-satellite solutions are now stable and ii) the reduction of the HY-2A scale offset after correction of the Center-Of-Mass Center-Of-Phase vector for that mission (according to DORISmail no 1092). The better stability of the single-satellite solution scales and consistency between it are the consequence of an important change in the ACs strategies from ITRF2014 to ITRF2020 processing (Štěpánek and Filler, 2018). Whereas for the ITRF2014 the data quality indicators were extracted from the DORIS data files, they are now estimated during the ACs preprocessing steps.

If we restrict the time period after mid-2002, from Table 5, we see that the IDS 16 scale is less scattered than with IDS 09. Over that time period, from Figure 7, we observe that the IDS 16 scale values lie in a range of ± 5 mm. The slope of the IDS 16 scale from mid-2002 to 2021.0 is about 0.062 mm/yr which corresponds to a linear increase of 1.15 mm over that time period. Moreover, the mean IDS 16 scale offset from mid-2002 to 2021.0 is about 9.82 mm, value which is comparable with the IDS 09 scale offset over the same time period and which was explained by the use of the Starec antenna PCV in the ITRF2014 processing. We remind the reader that such a scale offset is similar to the mean discrepancy ($8.4 - 10.2$ mm) between the two (SLR and VLBI) contributors to the ITRF2014 scale (Altamimi et al., 2016).

5.2. Translations

By looking at the translation parameters of Figure 9, a scatter reduction of IDS 16 vs IDS 09 is markedly evident. This is due to a reduction in

the amplitude of the annual signal by a factor of two. We also noticed a similar reduction of the amplitudes of the 118-day signal (corresponding to the first dracontic of the TOPEX and Jason satellites). These reductions are the result of a better modelling of the non-conservative forces on the Jason satellites. In addition, Figure 9 and Table 5 show that the scatter of the translations of the two series can be divided in three time periods (from 1993.0 to 2002.4; from 2004 to 2008.5 and after 2008.5) which corresponds to the inclusion of the second and third generation of DORIS receivers. That time decomposition with regards to the generation of the DORIS receivers is due to the increase of the number of the stations simultaneously received onboard (one for the first, two for the second and seven for the third generation). In addition to the evolution of the DORIS receivers capabilities, as indicated on top of Figure 1, these three time intervals also correspond to an increase of the number of DORIS missions simultaneously in flight. Moreover, we see that most of the IDS 09 and IDS 16 $x-$ and $y-$translations lie within the range $[-10; +10]$ mm. However, whereas the $x-$translations do not depict any no long-term trend/signal, the IDS 09 and IDS 16 $y-$translation depict, respectively, a 12.6 years (resp. 13.2 years) signal of amplitude 2.18 mm (resp. 2.75 mm). From Figure 9, we also observe a T_y increase in early 2016. According to the analysis of the single-satellite solutions from GRG (see Figure 10) and GSC, that pattern is the consequence of the linear increase of $y-$translations of the Cryosat-2, HY-2A, Saral and Sentinel-3A/B missions. Since such an increase is not visible on the $y-$translations of the Jason-2&3 missions, we suspect that an aspect of modeling for either the polar-orbiting or lower-altitude satellites might be the cause.

Additionally, from Figure 9 and Table 5, the $z-$translations of both IDS 09 and IDS 16 show similar performance and look highly correlated with the Sunspot number. Nevertheless, we observe a slight degradation of the IDS 16 T_z standard deviation after adding Jason-3 due to higher variations of that parameter for that mission. As reported in Bloßfeld et al. (2016), the correlation with the Sunspot number might be related to the modelling of the solar radiation pressure on the DORIS satellites and/or of the atmospheric drag due to the relation between the solar activity and the atmospheric density for the lower altitude DORIS satellites. Bloßfeld et al. (2016) also hypothesized that the highly correlation between the $z-$component and the Sunspot number could be the consequence of not including the second-order ionospheric correction in the IDS standards.

5.3. Station Position Residuals

Once the IDS 09 and IDS 16 series have been aligned to the ITRF2014 (by applying the Helmert parameters determined in sections 5.1 and 5.2), we have access to the weekly series of the station position residuals (differences between the IDS and ITRF2014 positions). Then, we can estimate the weekly WRMS (Weighted Root Mean Square - average value of weighted residuals using their formal errors) of the station position residuals.
From Figure 11 and Table 6, we notice that i) the IDS 16 station position residuals with respect to ITRF2014 are slightly better in both mean and STD values and over the three directions than for IDS 09, ii) the WRMS of both IDS 09 and IDS 16 are correlated to the number of DORIS satellites and iii) the IDS 16 residuals increase after 2015.0. The later observation is explained by the aging of ITRF2014. Since ITRF2014 included data through the end of 2014, this ITRF realization cannot account for position and/or velocity discontinuities (due for example to earthquakes) that occur after 2015.0. Thus, any significant position and velocity change observed at any station part of the IDS 16 series after 2015.0 will result as a residual increase. Furthermore, whereas the smallest residuals are observed in the North direction, the largest are for the East direction. This is the consequence of two features of the DORIS technique: i) the Doppler technique provides observations that lack information in the direction perpendicular to the satellite track and, ii) except for TOPEX/Poseidon, Jason-1/2/3, all the DORIS satellites have a near-polar orbit (see Table 3). Therefore, the best performance are expected to be in the South-North direction and the worst in the perpendicular direction to it: East-West.

5.4. EOP Performance

The IDS solution includes a complete series of daily polar motion parameters (P_x and P_y). The differences of these IDS X and Y pole components with respect to the IERS C04 pole series aligned to the ITRF2014 (Bizouard et al., 2019) are displayed by Figure 12. As with the translations and station position residuals, the precision of the EOP improves with the increase of the number of stations the DORIS onboard instrument can simultaneously receive: one until 2002.4 (including of the two first satellites with second generation of DORIS receiver: Envisat and SPOT-5), one to two up to mid-2008 (including of the first satellite with third generation of DORIS receiver: Jason-2) and one to seven afterwards. Comparisons of IDS 09 and IDS 16 polar motion solutions show a slight improvement of the IDS 16 differences w.r.t. the IERS C04 series (see Table 7). These comparisons also display

similar performance in the two directions thanks to the relatively homogeneous distribution of the DORIS tracking network.
The new series also displays lower formal errors for both $x-$ and $y-$pole estimations (see Figure 13 and Table 7). Note that the improved EOP performance of the IDS 16 series was obtained with two fewer contributors than for IDS 09. Furthermore, for the two IDS series, we observe an increase of the formal errors around 2002 which coincides with the peak of the solar activity for solar cycle 23 (cf. Figure 9) and so could be related to mismodeling in the atmospheric drag as suggested by Willis et al. (2005) and Gobinddass et al. (2010). However, unlike to the IDS 09, the formal errors of the IDS 16 series do not grow after the addition of HY-2A and stay stable at the order of $110 \pm 16\,\mu as$. From Table 7, we also see that the EOP formal errors are two to three times smaller than the EOP differences with respect to the IERS C04 values. Similar ratio numbers were observed for the individual IDS AC EOPs. Even if such discrepancies between formal errors and IERS C04 differences are also observed in GNSS products (Zajdel et al., 2020), some further investigations on potentially unmodelled errors will need to be undertaken by the IDS. Spectral analysis of IDS 16 EOPs differences with respect to IERS C04 series reveals that the largest amplitudes (with $86-87\,\mu as$) for the $x-$component are associated to annual and 118-120-day (draconitic period for TOPEX/Poseidon, Jason-1/2/3) signals. Note that these IDS 16 annual and 118-day amplitudes are slightly larger than the IDS 09 ones (amplitudes of both signals at $69-73\,\mu as$).

6. Internal evaluation of the IDS contribution to the ITRF2020

6.1. IDS 16 Cumulative Solution

To complete the evaluation of the IDS contribution to the ITRF2020, the IDS CC estimated a cumulative position and velocity solution from the 1456 IDS 16 weekly SINEX files. Due to the time evolution of the DORIS ground network, stations included in ITRF2014 may have been decommissioned and stations added to the tracking network after 2015.0 are, by definition, not part of ITRF2014. Thus, the evaluation with respect to the ITRF2014 is not well suited to provide a full picture of the station positioning performance of the IDS 16 series. In addition, any improvement in the SAA mitigation strategy between the IDS 09 and IDS 16 processing will be seen as degradation in the station positioning residuals with respect to the ITRF2014 since that solution rely on the IDS 09 solution.
The DORIS cumulative position and velocity solution is obtained by the stacking of all the weekly SINEX files into a long-term frame solution using

the CATREF (Combination and Analysis of Terrestrial Reference Frames) package from IGN. Each weekly terrestrial frame is aligned onto the long-term frame by estimating the seven Helmert transformation parameters (translations, rotations and scale). To overcome rank-deficiency of the normal equation system while computing the long-term frame, we apply internal constraints over the seven Helmert parameters. More details on the cumulative model are given in Appendix D. After removing from the weekly SINEX files sites with less than 2.5 years of observation (i.e. Ajaccio, Flores, Huanine, Lifou, Iquique, Ny-Ålesund II, San Juan, and Tana) to get reliable velocity estimations (Blewitt and Lavallée, 2002), the stacking process starts with the identification of coordinate jumps and velocity changes from the analysis of the station coordinate time series. The dates of the position and velocity discontinuities are compared with the list of earthquakes with possible impact on the DORIS stations as well as with the list of the station events (beacon change, antenna change, USO change...) as reported by the IDS[2]. From the IDS 16 coordinate time series, we identified 107 discontinuities at 41 DORIS sites (see Table 8): 58 associated with seismic events, 17 due to technical changes and 32 with still unknown origin. For comparison, if we limit the time interval up to the end of 2014 (ITRF2014 time span) then, we obtain 84 discontinuities (44 with seismic origin, 14 associated with a technical event and 26 with, so far, no explanation) at 38 sites. We also observe that more than 60 percent of the discontinuities since ITRF2014 have a seismic origin. Furthermore, we note that 14 of the 32 discontinuities with unknown origin are associated with DORIS stations located in the SAA region. In addition to the discontinuities, we make use of velocity constraints to force nearby stations or multiple segments of the same station to have the same velocity unless a velocity discontinuity was observed (e.g. due to an earthquake). The velocity equality/continuity constraints were also reviewed with the analysis of the velocities as output of the very first iteration which includes the station discontinuities but does not make use of any velocity constraint. We ended up with 157 velocity constraints at 58 sites. Thus, we obtained 296 horizontal and vertical velocities at 77 sites. Both horizontal and vertical velocities with errors smaller than 2.5 mm/yr are depicted by Figure 14 and 15.

The validation of the cumulative solution started with the analysis of the time series of the station position residuals (differences between the weekly

[2] `https://ids-doris.org/doris-system/system-monitoring/table-of-all-events.html`

estimates and the linear model as output of the stacking) and checked that the series had almost with no slope. Thanks to length of the DORIS site time span, to the relative small mean value of discontinuities per site and to the velocity constraints, more than 80 (resp. 90) percent of the 296 horizontal (resp. vertical) velocities have errors smaller than 1 mm/yr. In addition, to go further in the validation of the cumulative solution, we computed the DORIS-to-DORIS tie residuals: differences between the coordinate differences estimated from the cumulative solution and the surveyed ties delivered and regularly updated by IGN. Note that the tie vectors were not used as constraints in the computation of the cumulative solution. Therefore, the analysis of the tie residuals can be used as a benchmark of the quality of the cumulative solution. For the validation of the cumulative solution, we rejected pairs of stations separated by more than 500 m. Statistics of the tie residuals shown on Figure 16 are given in Table 10 and 3D ties larger than 15 mm are displayed on Figure 17. The three largest tie discrepancies are for DORIS sites located in the SAA region: Cachoeira, Tristan Da Cunha and Saint-Helena. These discrepancies may be the result of the remaining SAA effect on the station coordinates. Nonetheless, the RMS and median values of the tie residuals are smaller than 20 and 13 mm, respectively; values which are at the level of the ITRF2014 tie residuals as reported in Table 3 of Moreaux et al. (2019).

6.2. Internal scale and geocenter

As an output of the stacking of the IDS 16 series from 1993.0 to 2021.0, we get access to the weekly time series of the internal scale and geocenter. These series, depicted by Figure 18, correspond to the evaluation of the 1456 weekly SINEX files of the IDS 16 series with respect to the cumulative solution. While looking at the IDS 16 scale with respect to the ITRF2014 (see Figure 7) and the internal scale, we clearly see that the negative trend between 1993.0 and 2002.5 is no longer visible on the internal scale since firstly both the series and the reference use the same ground antenna PCVs and secondly due to the velocity equality constraints. Then, the internal scale series almost lies in a range of ± 5 mm over the full time period and exhibits a global trend of -0.008 mm/yr associtaed to a RMS value of 2.6 mm. Furthermore, the spectral analyis of the internal scale did not show any signal with amplitude larger than the mean parameter error (which had a value of 1.06 mm). Without any velocity equality constraint, the scale may be seen as a parabolic function of time with values in the range $[-10; +10]$ mm and with an inflection around 2005-2006, epoch which corresponds to the end of the use of the Alcatel ground antennas - see Figure 8).

The time series of the internal translations (see Figure 18) look very similar to the geocenter time series with respect to the ITRF2014 (see Figure 9) after removal of the global trend. The x, y, $z-$translations exhibit an overall trend of, respectively, 0.003, 0.002 and 0.015 mm/yr. Note that the centering and very small trends of the scale and translations over the full time span are the results of the internal constraints (see Eq. D.3). From Figure 18, we observe that both the $x-$ and $y-$translation time series lie within the range $[-10; +10]$ mm. Moreover, the spectral analysis of the internal translation parameters (see Figure 19) reveals that the three time series are dominated by annual signals of amplitudes of, respectively, 1.20, 1.70 and 3.20 mm. Nevertheless, only the annual signal of the z-translation is significant, i.e. is larger than the parameter mean error (1.37, 1.33 and 1.15 mm for the x, y, z-translations, respectively). In addition, the internal $z-$translation exhibits a clear and significant 118-day signal (first draconitic of the Jason satellites) with amplitude of 2.86 mm which may underline the needs for improvements in the modelling of the external forces like the solar radiation pressure on the Jason satellites.

6.3. Internal Positioning Performance

To get full access to the DORIS station positioning performance of the IDS 16 series, we can look at the position residuals as output of the cumulative solution estimation. These residuals are the differences between the weekly estimations from the SINEX files and the weekly positions derived from the linear motion model of the cumulative solution. Looking at the East, North and Up weekly WRMS of the station position residuals depicted by Figure 20 and summarized in Table 9, we first observe that the residuals can be divided in three time periods: from 1993.0 to mid-2002 (inclusion of the first satellite flying the second generation of DORIS receiver), from mid-2002 to mid-2008 (inclusion of the first satellite with the third generation of DORIS receiver) and mid-2008 afterwards. This time decomposition emphasizes the effect of having more and more stations simultaneously observed by the DORIS satellites, allowing more observations for each individual station. We can also notice that having since late 2015 a full constellation with onboard the third generation of DORIS receivers has only a very slight (but still) positive impact on the performance. Furthermore, in Figure 20, late 2020, we observe a slight increase of the WRMS in the East and North directions. These increases are the results of missing of some earthquakes in our discontinuity list due to very short period of time until the end of the ITRF2020 data interval. Nonetheless, since the start of Jason-2 in mid-2008, the East, North and Up the station position residuals are smaller than 7.5 mm. After all, we

analyzed the geographical distribution of the 3D-RMS position residuals for the years 2000, 2007, 2014 and 2019. We selected these four years since they represent four distinct stages in the evolution of the DORIS constellation (see Table 3): in 2000 all the DORIS receivers had one channel (i.e. could track only one station at a time) while in 2007 (resp. 2014) the constellation contained a majority of DORIS receivers with 2 (resp. 7 channels) and, in 2019 all the missions were equipped with 7-channel receivers. That analysis shows that i) the residuals decrease with time, ii) the residuals are smaller at higher latitudes due to a higher number of observations (as a result of the DORIS mission orbit inclinations) as well as due to larger troposphere modelling errors for the equatorial region, iii) the differences between the 3D RMS with regards to the latitude of the sites decrease with time (due to an increasing number of missions simultaneously in operation and of the capability of the third version of the DORIS instruments to receive more stations, especially at low elevations) and iv) the DORIS sites located in the SAA region still exhibit the largest residuals.

7. Conclusions

In total 1456 weekly solution files for the IDS contribution to the ITRF2020, covering the time period from 1993.0 to 2021.0, were submitted to the IERS. These weekly files include weekly DORIS station positions of, in overall, 201 stations at 87 sites and daily X and Y pole coordinates. Note that around one third of the DORIS sites exhibit coordinate time series longer than 20 years. The IDS contribution to the ITRF2020 is the result of the combination of four IDS AC solutions derived using four distinct orbit determination programs (see Table 1 and 2) which include the latest IERS and IDS standards. Among the new IDS standards we can cite the new Alcatel ground antenna phase center variation model and the mitigation strategies of the South Atlantic Anomaly on the DORIS onboard receiver frequencies as described in Section 2.

Compared to the IDS contribution to the ITRF2014, the IDS ITRF2020 solution exhibits a scale slope between 1993.0 and mid-2002 with respect to the ITRF2014 (see Section 5). This IDS 16 scale slope is due to the use of different Alcatel PCVs between ITRF2014 and ITRF2020 combined with gradual replacement over time of the Alcatel by Starec ground antennas (see Section 5.1). After mid-2002, compared to the IDS 09, the IDS 16 scale is more stable thanks to the correction of the HY-2A Center-Of-Mass Center-Of-Phase vector and to a new weighting strategy of the IDS AC contributions between 2005 and 2012 depending on their Jason-2 weighting. Furthermore, the scale

of the IDS 16 series is less sensitive to the sawtooth pattern of the SPOT-5 scale after the IDS recommended to not include the contribution of that mission to the scale of the AC multi-satellite solutions. Nevertheless, the IDS 16 (as IDS 09) scale displays some slight variations (up to 5 mm maximum) correlated with the time evolution of the DORIS constellation. Comparison of the IDS 16 with the ITRF2014 shows a mean scale offset from mid-2002 to 2021.0 of 9.82 mm and values within the range $[5; 15]$ mm. Since these IDS 16 offset values are at the level of the SLR-VLBI scale discrepancy observed in the elaboration of the ITRF2014 ($8.4 - 10.2$ mm reported by Altamimi et al., 2016), the IDS 16 may compete to the ITRF2020 scale definition.

Thanks to a better modeling of the solar radiation pressure forces on the DORIS satellites, compared to the IDS 09 series, the IDS 16 geocenter shows smaller annual and Jason first draconitic (i.e. 118-day) signals. Nonetheless, the IDS 16 $y-$component of the geocenter exhibits an increase early 2016 which was associated to the linear increases of that parameter for the Cryosat-2, HY-2A and Sentinel-3A&B single-satellite solutions. Upcoming analysis of all the IDS AC single-satellite solutions will provide the opportunity to make further investigations on the IDS geocenter and scale. EOP comparisons between the IDS 09 and IDS 16 series differences with respect to the IERS C04 series reveal similar performance. We also observe a reduction by a factor of three of the X and $Y-$pole scatter between the 1990's and the inclusion of the first mission with onboard the third generation of the DORIS receivers (Jason-2, mid-2008). Note that the IDS 16 series relies on two contributors less than IDS 09 (4 vs 6).

Due to the aging of the ITRF2014, to assess the positioning performance of the IDS 16 series, we looked at the position residuals as the output of the estimation of an IDS 16 position and velocity cumulative solution from 1993.0 to 2021.0 (see Section 6). The time series of the North, East and Up residuals (differences between the weekly estimations and the linear motion models) are improved when more satellites are available and show the impact of the addition in mid-2002 and mid-2008 of the first missions with onboard the second and third generation of DORIS receivers. This latter impact is the consequence of the increasing number of stations simultaneously observed. In addition, we note that over the time period since the end of the ITRF2014, the residuals still decrease thanks to the new missions (Jason-3, Sentinel-3A&B). Thus, in overall, the WRMS of the ENU position residuals are below $6 - 7$ mm since mid-2008. Despite the improvements by the IDS ACs in the mitigation of the SAA on the DORIS missions, the largest residuals remain for the DORIS stations located close to South America.

In addition to the integration of the new (Jason-CS/Sentinel-6A and HY-2C)

and forthcoming (SWOT, HY-2D) missions, the post-ITRF2020 IDS combined series will benefit of the return to operation of the IGN and INASAN ACs. In a near future, the IDS combined series may also take advantage of the addition of, at least, one of the two IDS associated analysis center solutions. In parallel, the continuing deployment of the fourth generation of DORIS beacons with less stringent constraints on the distance between the antenna and the beacon will contribute to the continuous improvement on the IDS products (station coordinate time series, Earth Orientation Parameter time series) and by-products (DPOD).

Acknowledgments

Part of this work was performed at CLS under contract with the Centre National d'Etudes Spatiales (CNES) and at GOP AC contribution was supported by the grant LTT18012 of Czech ministry of Education, Youth and Sports. The NASA GSFC DORIS Analysis Center contribution to ITRF2020 was supported by the NASA Space Geodesy Project (SGP). The authors are grateful to all the Agencies hosting DORIS stations. All the data used in this study are freely available and downloadable from the IDS data centers: CDDIS (`https://cddis.nasa.gov/archive/doris/`)and IGN (`ftp://doris.ign.fr/pub/doris/`).

References

Altamimi, Z., Boucher, C., & Sillard, P. New trends for the realization of the international terrestrial reference system. Adv. Space Res. 30(2), 175-184, doi:10.1016/S0273-1177(02)00282-X, 2002a.

Altamimi, Z., Sillard, P. & Boucher, C. ITRF2000: A new release of the International Terrestrial Reference Frame for earth science applications. J. Geophys. Res., 107 (B10), 2214, doi:10.1029/2001JB000561, 2002b.

Altamimi, Z., Collilieux, X., Legrand, J., et al. ITRF2005: A new release of the International Terrestrial Reference Frame based on time series of station positions and Earth Orientation Parameters. J. Geophys. Res., 112(B9), doi:10.1029/2007JB004949, 2007.

Altamimi Z., Rebischung P., Metivier P., et al. ITRF2014: A new release of the International Terrestrial Reference Frame modeling nonlinear station motions. J Geophys Res, vol 121(8), 6109-6131, doi: 10.1002/2016JB013098, 2016.

Auriol, A., & Tourain, C. DORIS system: The new age. Adv. Space Res., 46(12), 1484-1496, doi:10.1016/j.asr.2010.05.015, 2010.

Belli, A., Zelensky, N.P., Lemoine, F.G., et al. Impact of Jason-2/T2L2 Ultra-Stable-Oscillator Frequency Model on DORIS stations coordinates and Earth Orientation Parameters. Adv. Space Res., 67(3), 930-944, doi: 10.1016/j.asr.2020.11.034, 2021.

Bird, P. An updated digital model of plate boundaries. Geochem. Geophys. Geosys. 4(3), 1027. doi:10.1029/2001GC000252, 2003.

Bizouard, C., Lambert, S., Gattano, C., et al., The IERS EOP 14C04 solution for Earth orientation parameters consistent with ITRF 2014. J. Geod., 93(5), 621-633, doi:10.1007/s00190-018-1186-3, 2019.

Blewitt, G., & Lavallée, D. Effect of annual signals on geodetic velocity. J. Geophys. Res., 107(7), doi: 10.1029/2001JB000570, 2002.

Bloßfeld, M., Seitz, M., Angermann, D., et al. Quality assessment of the IDS contribution to ITRF2014 performed by DGFI-TUM. Adv. Space Res., 58(12), 2505-2519, doi: 10.1016/j.asr.2015.12.016, 2016.

Capdeville, H., Štěpánek, P., Lemoine, J.-M., et al. Update of the corrective model for Jason-1 DORIS data in relation to the South Atlantic Anomaly and a corrective model for Spot-5. Adv. Space Res., 58(12), 2628-2650, doi: 10.1016/j.asr.2016.02.009, 2016.

Capdeville, H., Lemoine, J.M., Mezerette, A., et al. Activity of the CNES/CLS Analysis Center for the IDS contribution to ITRF2020.

Desai, S.D. Observing the pole tide with satellite altimetry. J. Geophys. Res., 107(C11), 3186, doi:10.1029/2001JC001224, 2002.

Dobslaw, H., Bergmann-Wolf, I., Dil,l R., et al. A new high-resolution model of non-tidal atmosphere and ocean mass variability for de-aliasing of satellite gravity observations: AOD1B RL06, Geophys. J. Int., 211, 263-269, doi:10.1093/gji/ggx302, 2017.

Fagard, H. Twenty years of evolution for the DORIS permanent network from its initial deployment to its renovation. J. Geod, 80(8-11), 429-456, doi:10.1007/s00190-006-0084-2, 2006.

Gobinddass, M.L., Willis, P., Menvielle, M., et al. Refining DORIS atmospheric drag estimation in preparation of ITRF2008. Adv. Space Res., 46(12), 1566-1577, doi:10.1016/j.asr.2010.04.004, 2010.

Jalabert, E., & Mercier, F. Analysis of South Atlantic Anomaly perturbations on Sentinel-3A Ultra Stable Oscillator. Impact on DORIS phase measurement and DORIS station positioning. Adv. Space Res, 62(1), 174-190, doi:10.1016/j.asr.2018.04.005, 2018.

Lemoine, J.-M., & Capdeville, H. A corrective model for Jason-1 DORIS Doppler data in relation to the South Atlantic Anomaly. J. Geod. 80(8–11), 507-523, doi:10.1007/s00190-006-0068-2, 2006.

Lemoine, J.-M., Capdeville, H., Soudarin, L. Precise orbit determination and station position estimation using DORIS RINEX data. Adv. Space Res., 58(12), 2677-2690, doi: 10.1016/j.asr.2016.06.024, 2016.

Lyard, F., Damien, J.D., Cancet, M., et al. FES2014 global ocean tides atlas: design and performance, Ocean Sci., 17, 615–649, doi:10.5194/os-2020-96, 2021.

Mayer-Gürr, T., Kvas, A., Rieser, D., et al. The combined satellite gravity field model GOCO05s. EGU General Asembly 2015, Abstract EGU2015-12364, Vienna, Austria, April 12-17, 2015.

Moreaux G., Lemoine F. G., Capdeville H., et al. The International DORIS Service contribution to the 2014 realization of the International Terrestrial Reference Frame. Adv. Space Res., 58(12), 2479-2504, doi:10.1016/j.asr.2015.12.021, 2016.

Moreaux, G., Willis, P., Lemoine, F.G., et al. DPOD2014: a new DORIS extension of ITRF2014 for Precise Orbit Determination. Adv. Space Res., 63(1), 118-138, doi: 10.1016/j.asr.2018.08.043, 2019.

Noll, C., & Soudarin, L. On-line ressources supporting the data, products, and information infrastructure for the International DORIS Service. J. Geod, 80(8-11), 419-427, doi:10.1007/s00190-006-0051-y, 2006.

Petit, G., & Luzum, B. IERS Conventions (2010), IERS Technical Note 36 Verlag des Bundesamts für Kartographie und Geodäsie, Frankfurt am Main, 2011.

Ray, R. D. Precise comparisons of bottom-pressure and altimetric ocean tides, J. Geophys. Res. Oceans, 118, 4570–4584, doi:10.1002/jgrc.20336, 2013.

Ray,R .D., & Ponte, R.M. Barometric tides from ECMWF operational analyses. Ann. Geophys., 21, 1897-1910, doi:10.5194/angeo-21-1897-2003, 2003.

Ries, J.C., Petit, G., & Luzum, B. What does the 'mean pole' mean?, American Geophysical Union Fall Meeting, Paper 74451, San Francisco, California, U.S.A., December 14-18, 2015.

Ries, J.C., & Desai, S.D. Conventional model update for rotational deformation, American Geophysical Union Fall Meeting, Paper 290906, New Orleans, Louisiana, U.S.A., December 11-15, 2017.

Saastamoinen, J. Atmospheric correction for the troposphere and stratosphere in radio ranging of satellite. Geophysical Monograph 15: The Use of Artificial Satellites for Geodesy. American Geophysical Union, Washington DC, doi:10.1029/GM015p0247, 1972.

Saunier, J. The DORIS network: advances achieved in the last fifteen years. Adv. Space Res, submitted

Sillard, P. Modélisation des systèmes de référence terrestres. PhD thesis, Obserbatoire de Paris, 1999.

Štěpánek, P., &, Filler, V. Cause of scale inconsistencies in DORIS time series. Stud. Geophys. Geod., 62(4), 562-585, doi: 10.1007/s11200-018-0406-X, 2018.

Štěpánek, P., Bingbing, D., Filler, V., et al. Inclusion of GPS clock estimates for satellites Sentinel-3A/3B in DORIS geodetic solutions. J. Geod, 94, 116, doi: 10.1007/s00190-020-01428-x, 2020.

Štěpánek, P., &, Filler, V. DORIS Alcatel ground antenna: Evaluation of the phase center variation models. Adv. Space Res, in press, doi:10.1016/j.asr.2022.02.024, 2022.

Štěpánek, P., Hugentobler, U., Filler, V., et al. The GOP Analysis Center DORIS contribution to ITRF2020. Adv. Space Res, submitted.

Tourain, C., Moreaux, G., Auriol, A., et al. Doris starec ground antenna characterization and impact on positioning. Adv. Space Res., 58(12), 2707-2716, doi:10.1016/j.asr. 2016.05.013, 2016.

Valette, J.-J., Lemoine, F.G., Ferrage, P., et al. IDS contribution to ITRF2008. Adv. Space Res., 46(12), 1614-1632, doi:10.1016/j.asr.2010.05.029, 2010.

Willis, P., Haines, B., & Berthias, J.-P. Behavior of the DORIS/Jason oscillator over the South Atlantic Anomaly. C.R. Geosci. 336(9), 839-846, doi: 10.1016/j.crte.2004.01.004, 2004.

Willis, P., Deleflie, F., Barlier, F., et al. Effects of thermosphere total density perturbations on LEO orbits during severe geomagneticconditions (Oct-Nov 2003) using DORIS and SLR data. Adv. Space Res., 36 (3), 522-533, doi:10.1016/j.asr.2005.03.029, 2005.

Willis, P. Analysis of a possible future degradation of the DORIS results related to changes in the satellite constellation. Adv. Space Res., 39(10), 1582-1588, doi: 10.1016/j.asr.2006.11.018, 2007.

Willis, P., Haines, B.J., & Kuang, D. DORIS satellite phase center determination and consequences on the derived scale of the Terrestrial Reference Frame. Adv. Space Res., 39(10), 1589-1596, doi: 10.1016/j.asr.2007.01.007, 2007.

Willis, P., Fagard, H., Ferrage, P., et al. The International DORIS Service (IDS), Toward maturity. Adv. Space Res., 45(12), 1408-1420, doi: 10.1016/j.asr.2009.11.018, 2010.

Willis, P., Helfin, M.B., Haines, B.J., et al. Is the Jason-2 DORIS oscillator also affected by the South Atlantic Anomaly? Adv. Space Res., 58(12), 2617-2627, doi: 10.1016/j.asr.2016.09.015, 2016.

Zajdel, R., Sośnica, K., Bury, G., et al. System-specific systematic errors in earth rotation parameters derived from GPS, Glonass, and Galileo. GPS Solut., 24, 74, doi: 10.1007/s10291-020-00989-w, 2020.

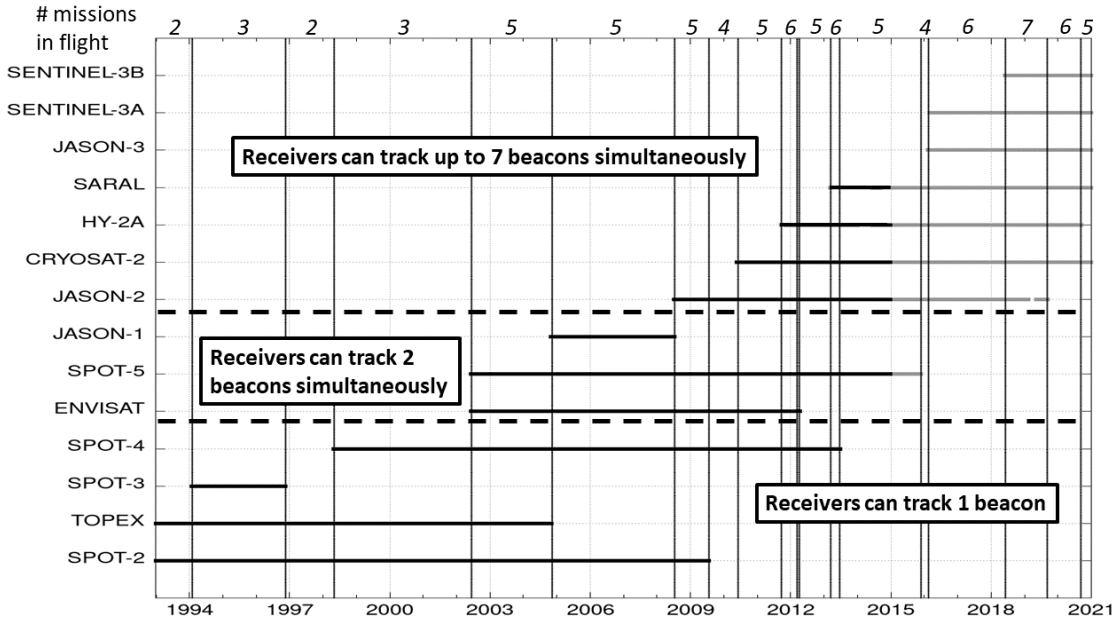

Figure 1: Time evolution of the DORIS constellation for ITRF2020 (black = ITRF2014 constellation; black + grey = ITRF2020 constellation). Vertical lines correspond to starting and ending dates of the DORIS missions.

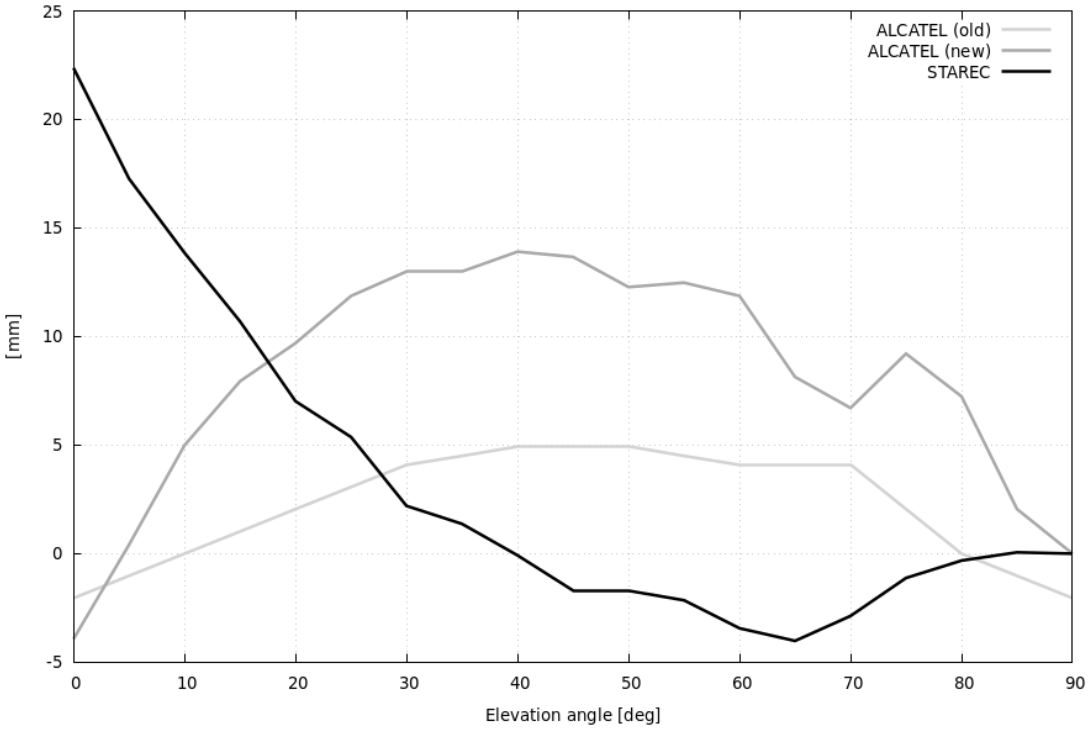

Figure 2: Starec (black) and Alcatel (light gray: old - ITRF2014; gray: new - ITRF2020) DORIS antenna phase laws.

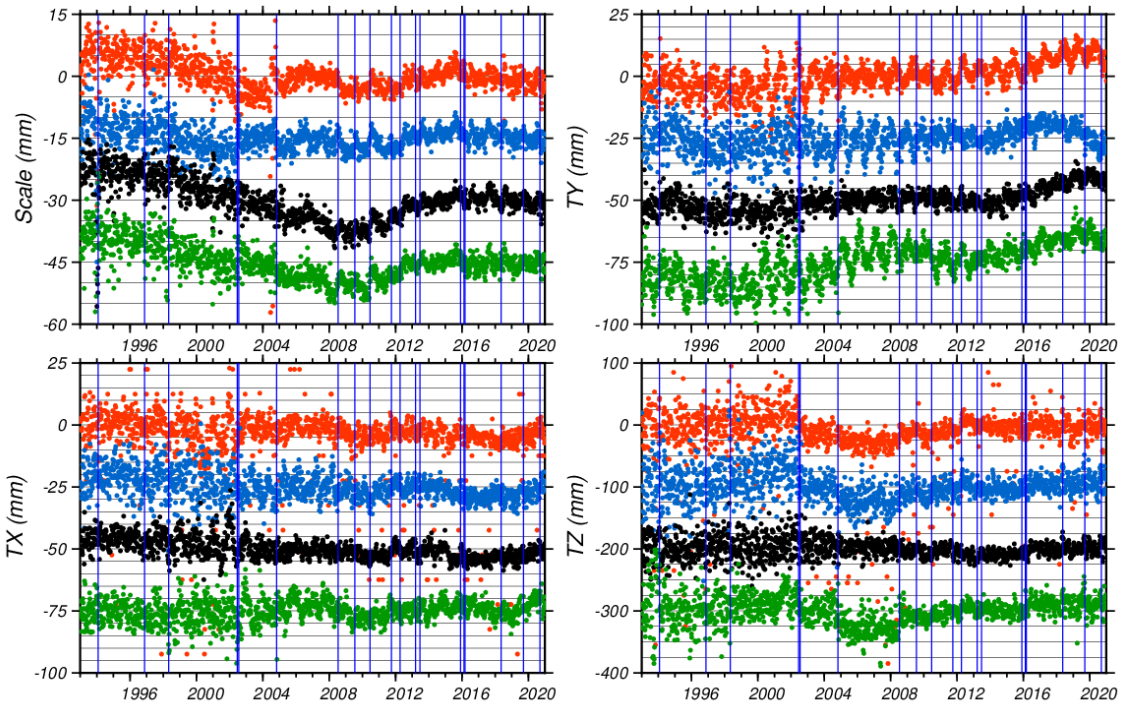

Figure 3: Geocenter and scale with respect to ITRF2014 of the IDS AC solutions for the ITRF2020 (red: ESA, blue: GOP, black: GRG and green: GSC). Each solution was shifted for a better viewing. Vertical lines correspond to DORIS satellite constellation changes.

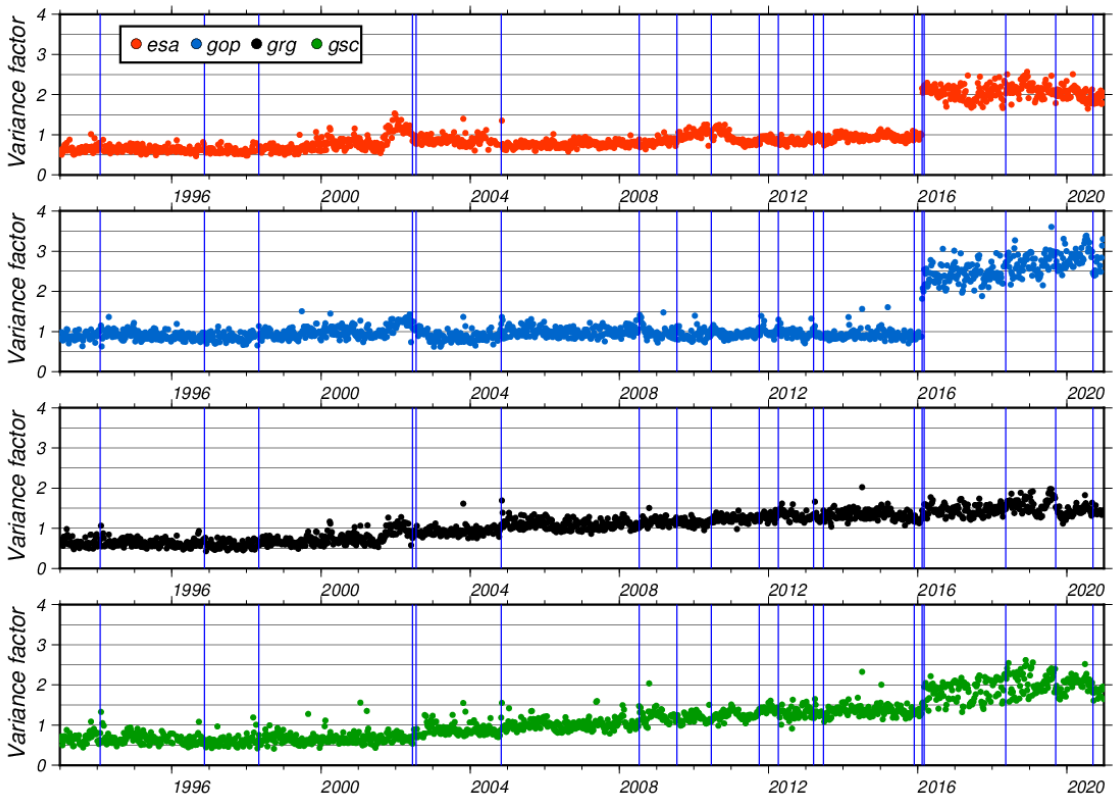

Figure 4: Weekly variance factor of the IDS AC contributions to the IDS 16 series (from top to bottom: ESA, GOP, GRG and GSC). Vertical lines correspond to DORIS satellite constellation changes.

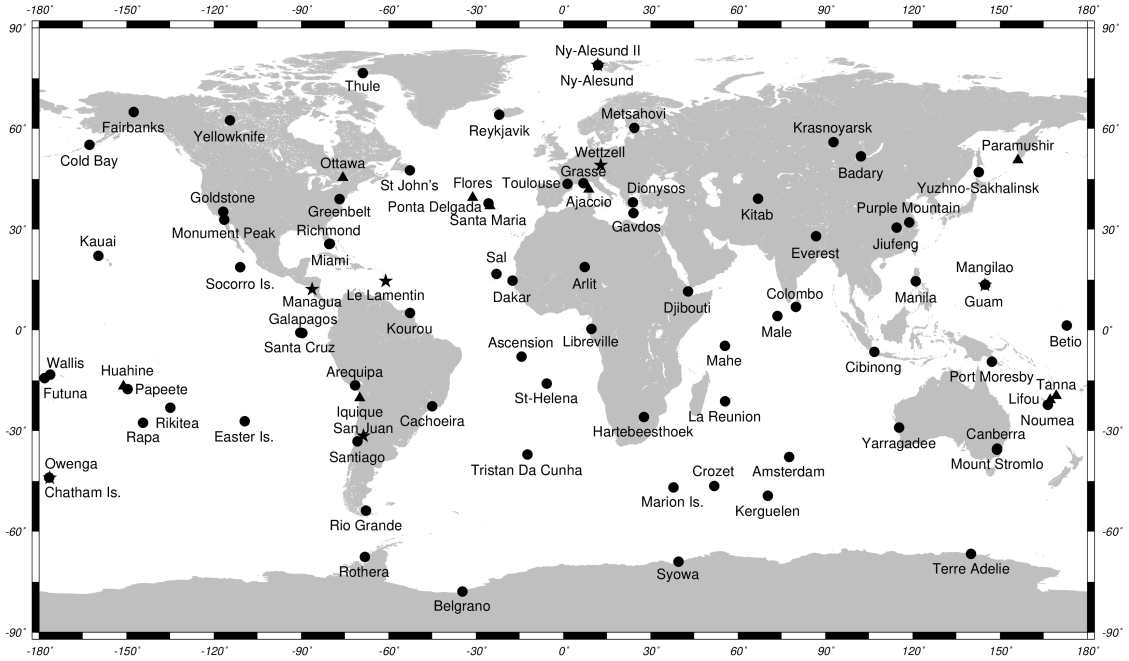

Figure 5: Geographical distribution of the DORIS stations included in the IDS contribution to the ITRF2020 (stars indicate new sites installed since 2015.0 and triangles old sites not included in the ITRF2014).

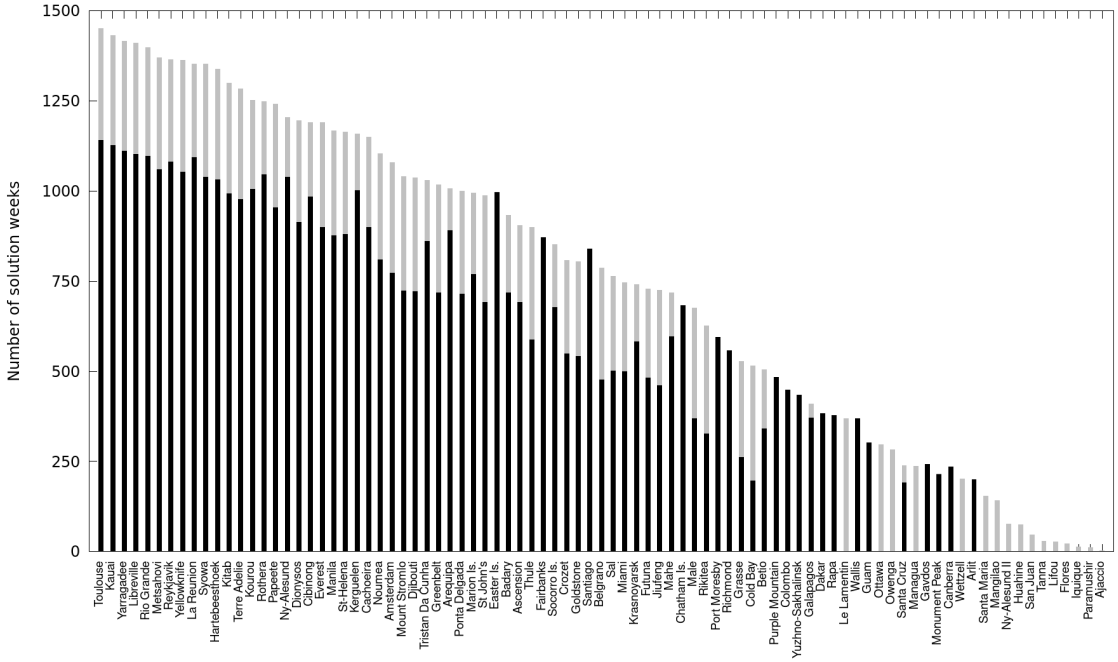

Figure 6: Number of weeks of sites positions in IDS contribution to both ITRF2020 (IDS 16 - grey) and ITRF2016 (IDS 09 - black).

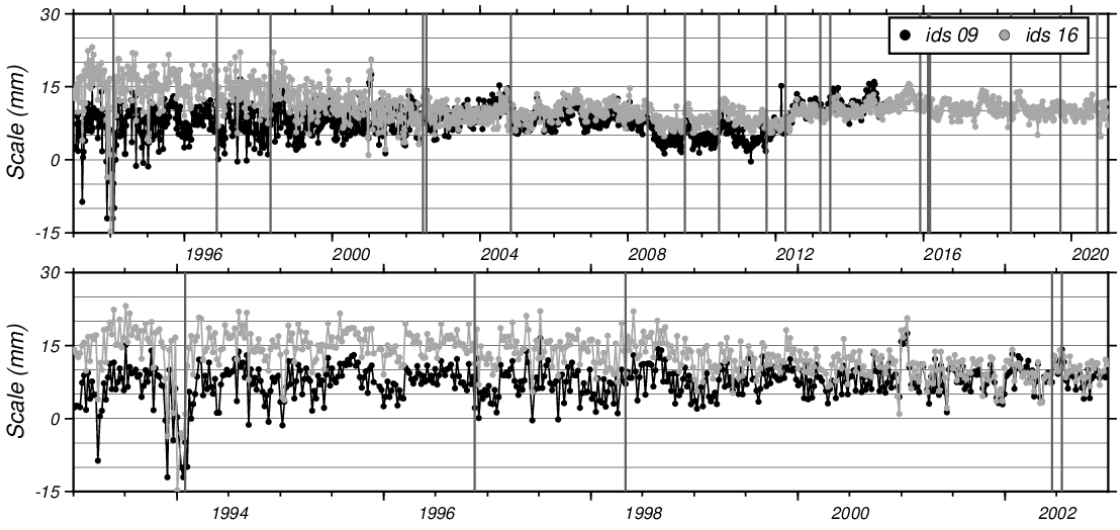

Figure 7: Scale with respect to ITRF2014 of IDS 09 (ITRF2014) and IDS 16 (ITRF2020) series from 1993.0 to 2021.0 (Top) and zoom from 1993.0 to 2003.0 (Bottom). Vertical lines correspond to DORIS satellite constellation changes.

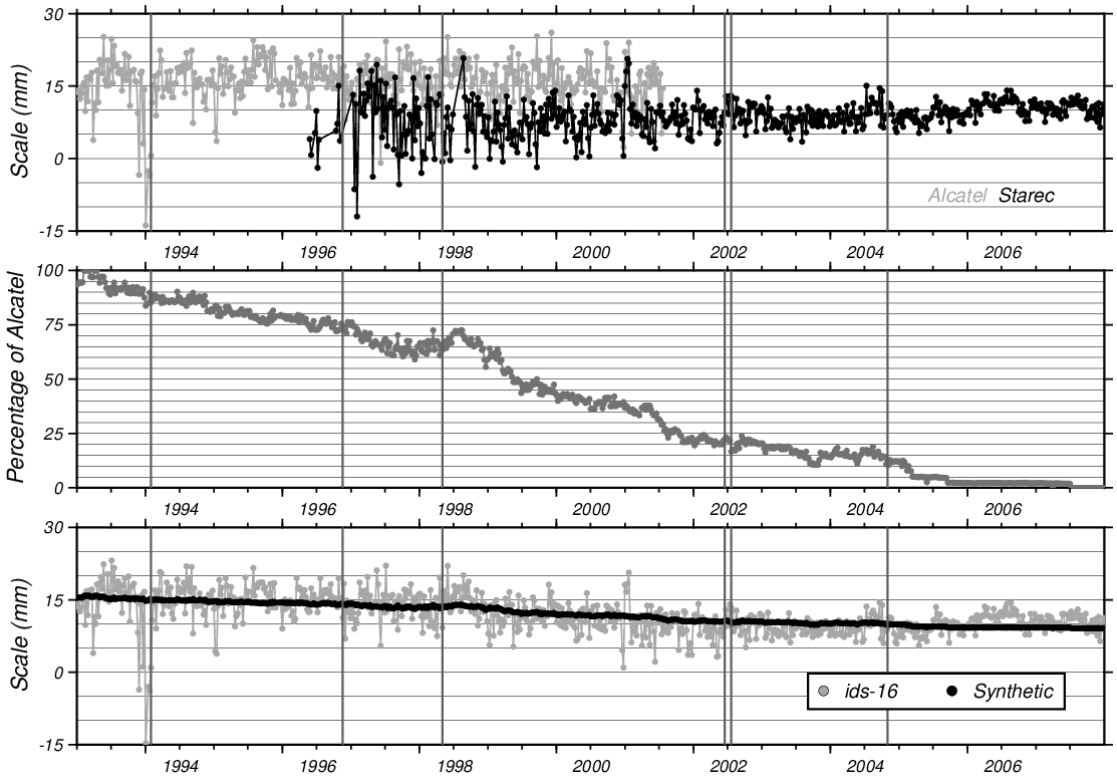

Figure 8: Top: Scale with respect to ITRF2014 of IDS 16 (ITRF2020) series with either Alcatel or Starec antenna network only. Middle: time evolution of the percentage of Alcatel antennas in the DORIS ground network. Bottom: IDS 16 and synthetic (combination of the Alcatel and Starec mean scale values and the percentage of Alcatel antennas) scales with respect to ITRF2014. Vertical lines correspond to DORIS satellite constellation changes.

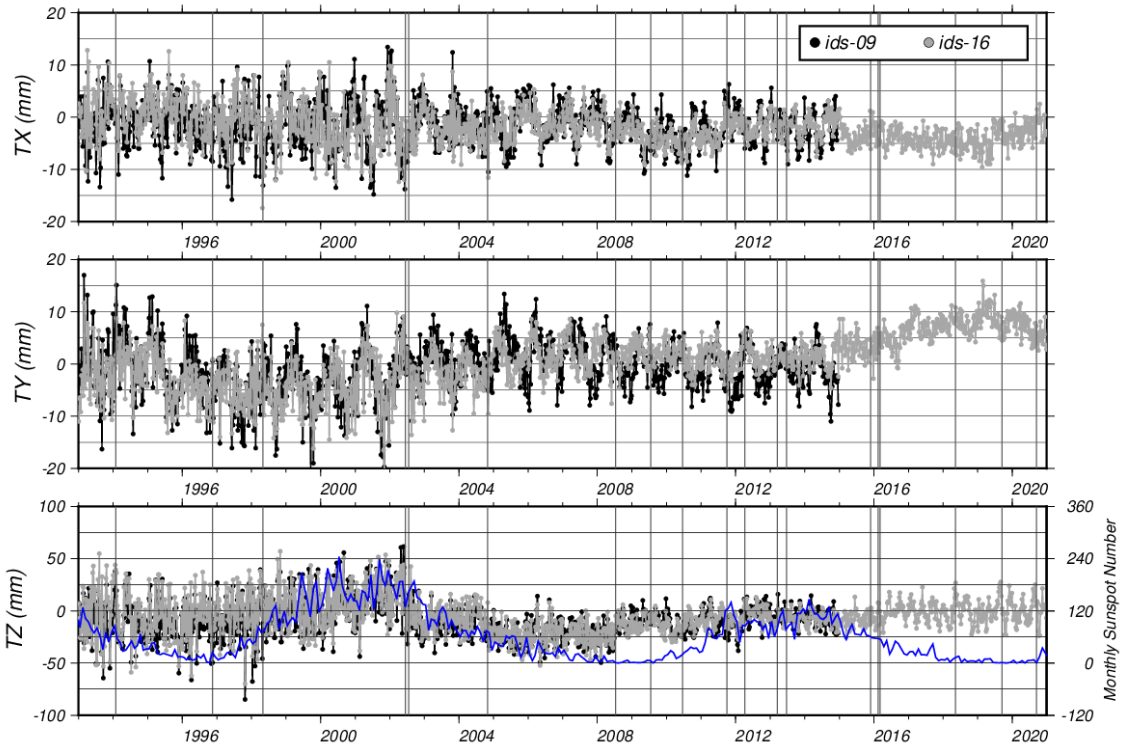

Figure 9: Geocenter with respect to ITRF2014 of IDS 09 (ITRF2014) and IDS 16 (ITRF2020) series. Vertical lines correspond to DORIS satellite constellation changes. In addition to the z-translation, also the Sunspot number (in blue) from the WDC SILSO, Royal Observatory of Belgium, Brussels.

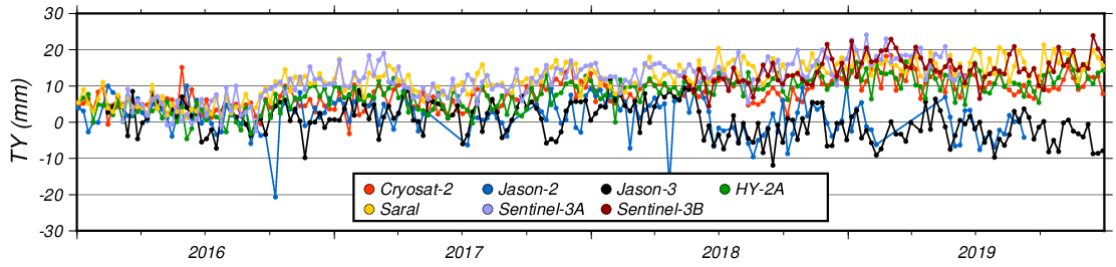

Figure 10: $y-$translation with respect to ITRF2014 of the single-satellite solutions from GRG IDS AC from 2016.0. to 2020.0

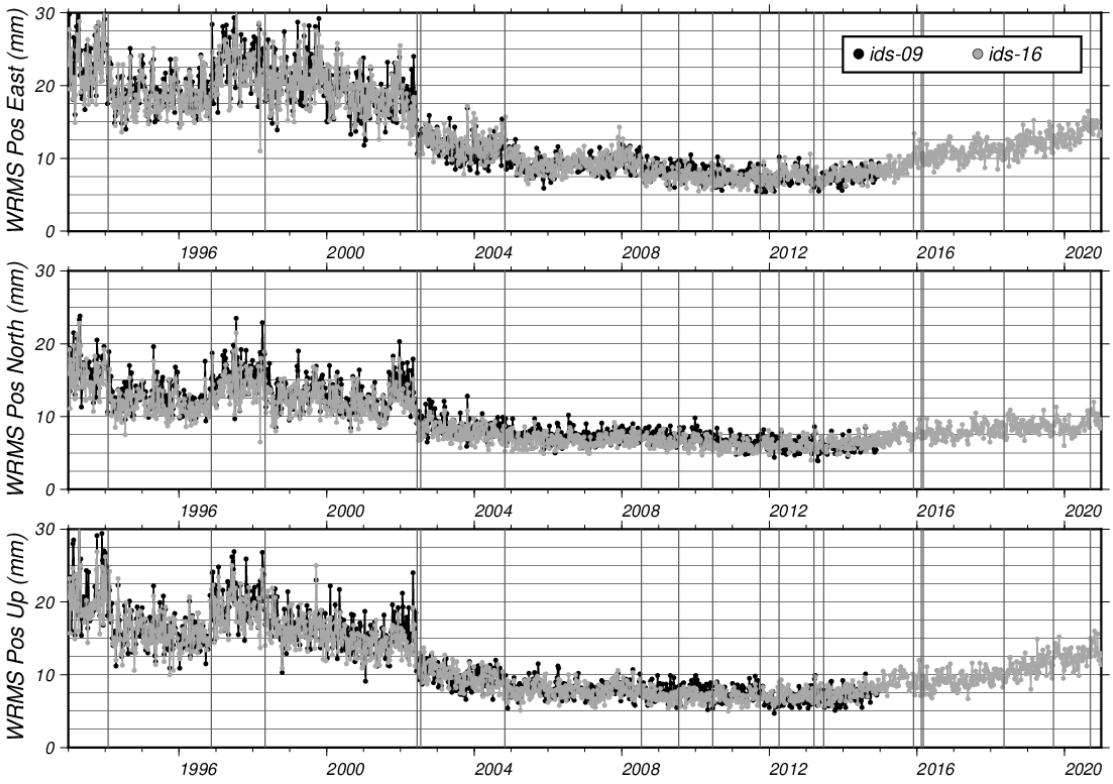

Figure 11: Weighted RMS of station position residuals with respect to ITRF2014 of IDS 09 (ITRF2014) and IDS 16 (ITRF2020) series. Vertical lines correspond to DORIS satellite constellation changes.

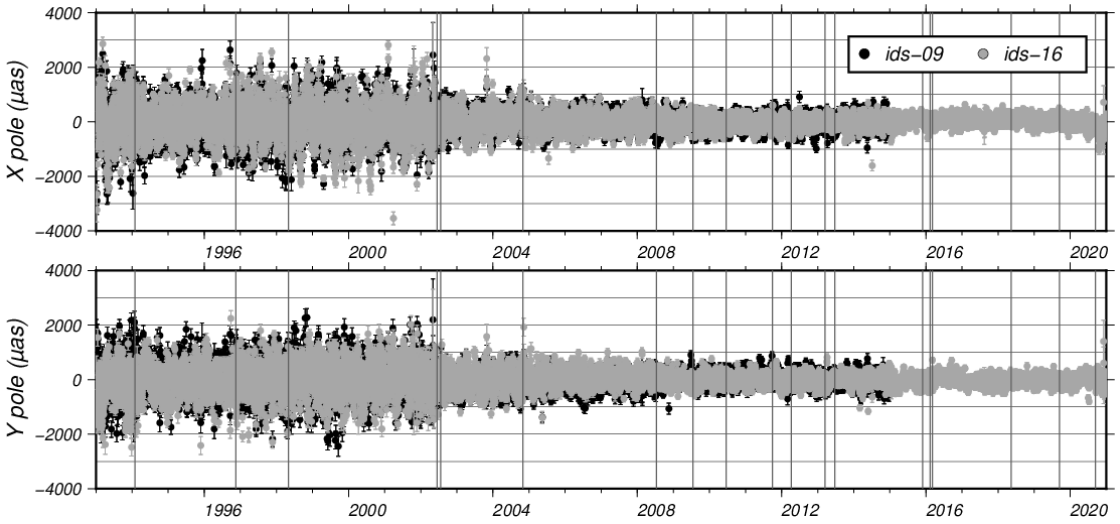

Figure 12: IDS 09 (ITRF2014) and IDS 16 (ITRF2020) polar motion compared to IERS C04 series. Vertical lines correspond to DORIS satellite constellation changes.

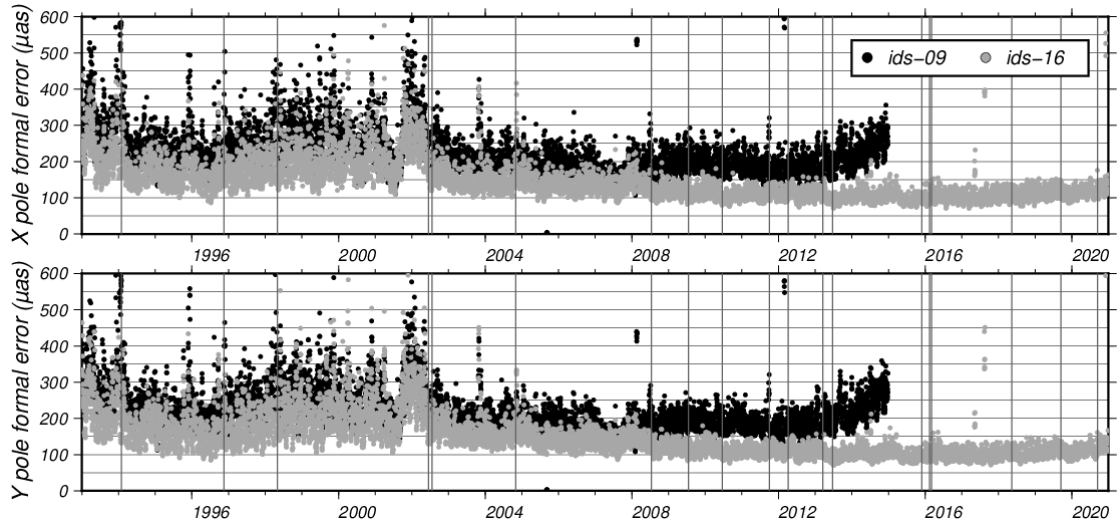

Figure 13: IDS 09 (ITRF2014) and IDS 16 (ITRF2020) polar motion formal errors. Vertical lines correspond to DORIS satellite constellation changes.

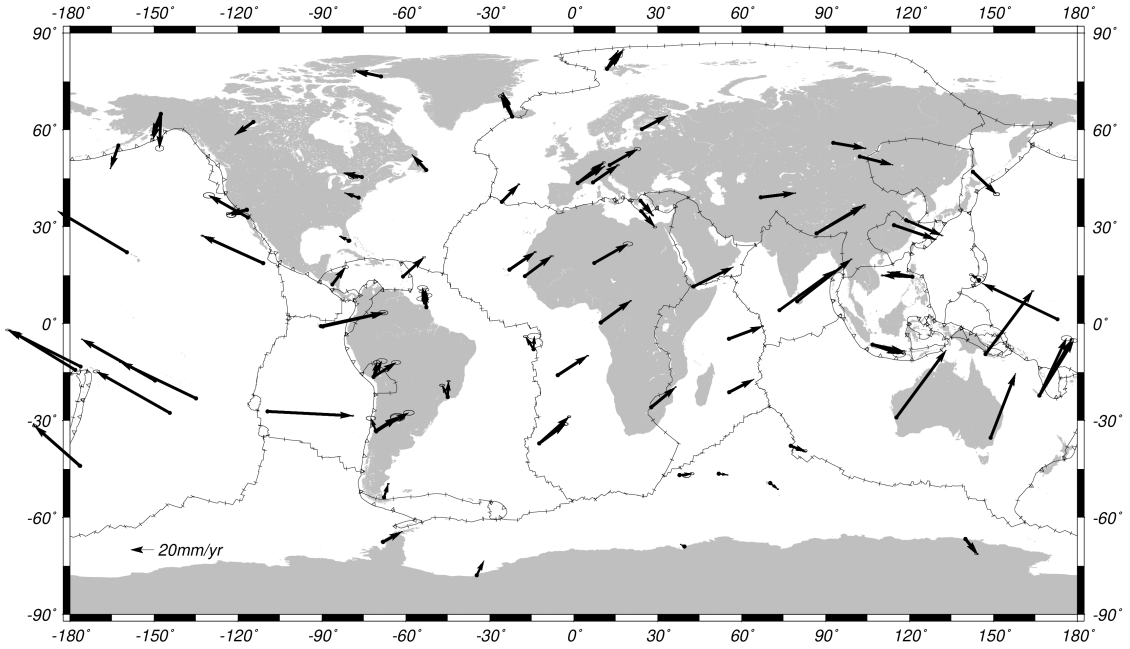

Figure 14: Horizontal velocities of DORIS sites from IDS 16 cumulative solution with formal error less than 2.5 mm/yr. Plate boundaries are shown according to Bird (2003).

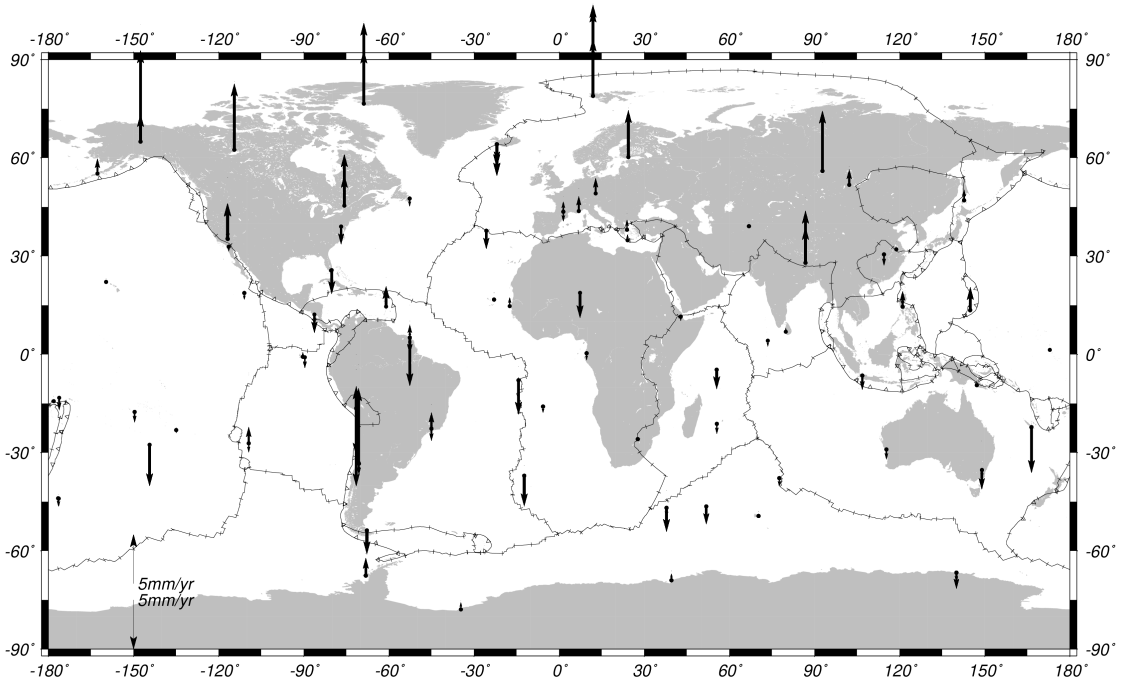

Figure 15: Vertical velocities of DORIS sites from IDS 16 cumulative solution with formal error less than 2.5 mm/yr. Plate boundaries are shown according to Bird (2003).

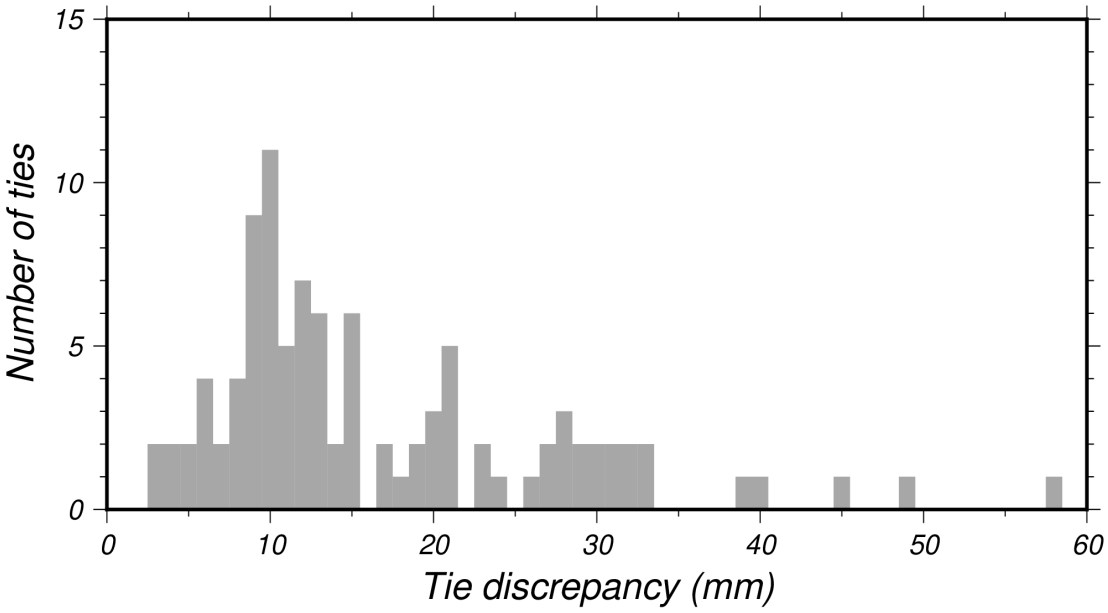

Figure 16: Histogramm of the 3D tie residuals between the IDS 16 cumulative solution and the DORIS-to-DORIS surveyed ties.

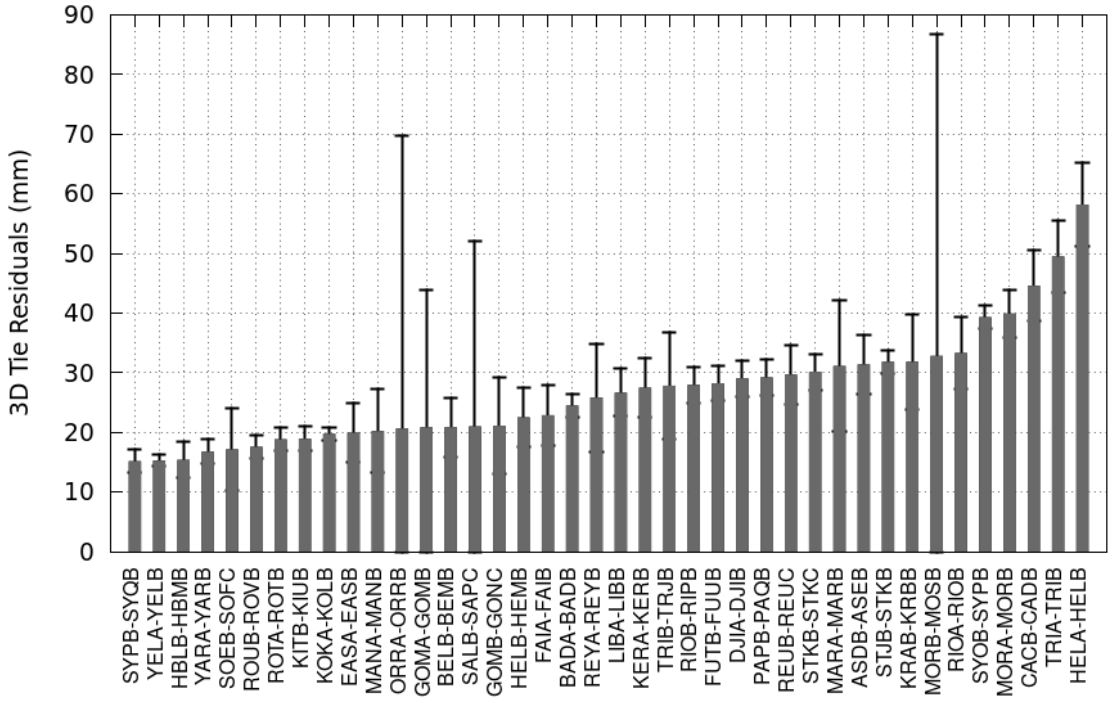

Figure 17: 3D tie residuals between the IDS 16 cumulative solution and the DORIS-to-DORIS surveyed ties. The black vertical bars represent the 3D formal errors of the station positions. We only show tie residuals larger than 15 mm.

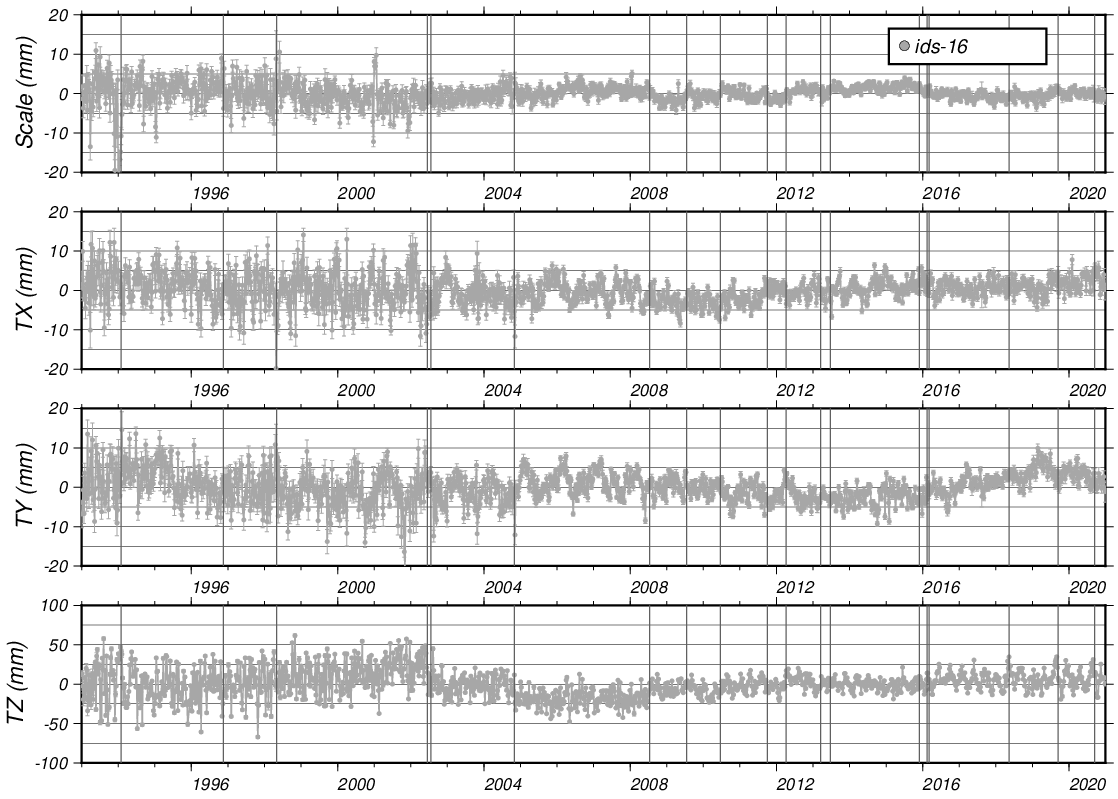

Figure 18: Internal scale and geocenter of the IDS 16 series (IDS contribution to the ITRF2020).

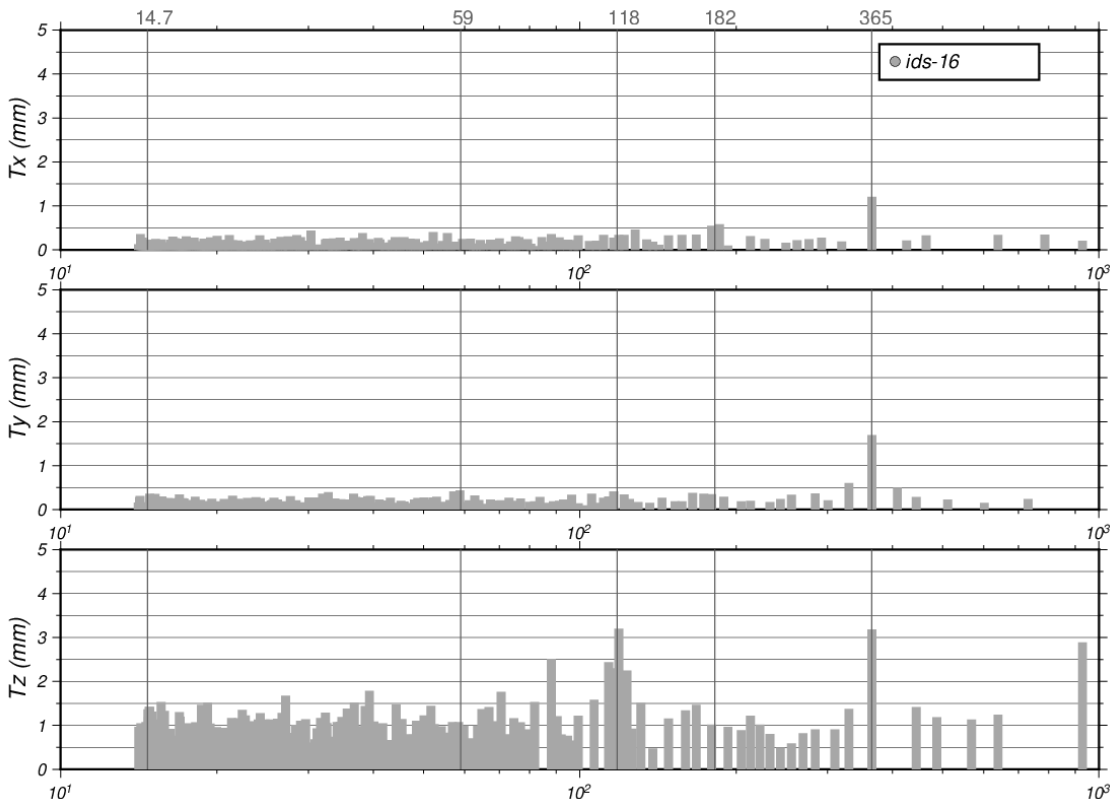

Figure 19: Spectra of the translation parameter time series of Figure 18.

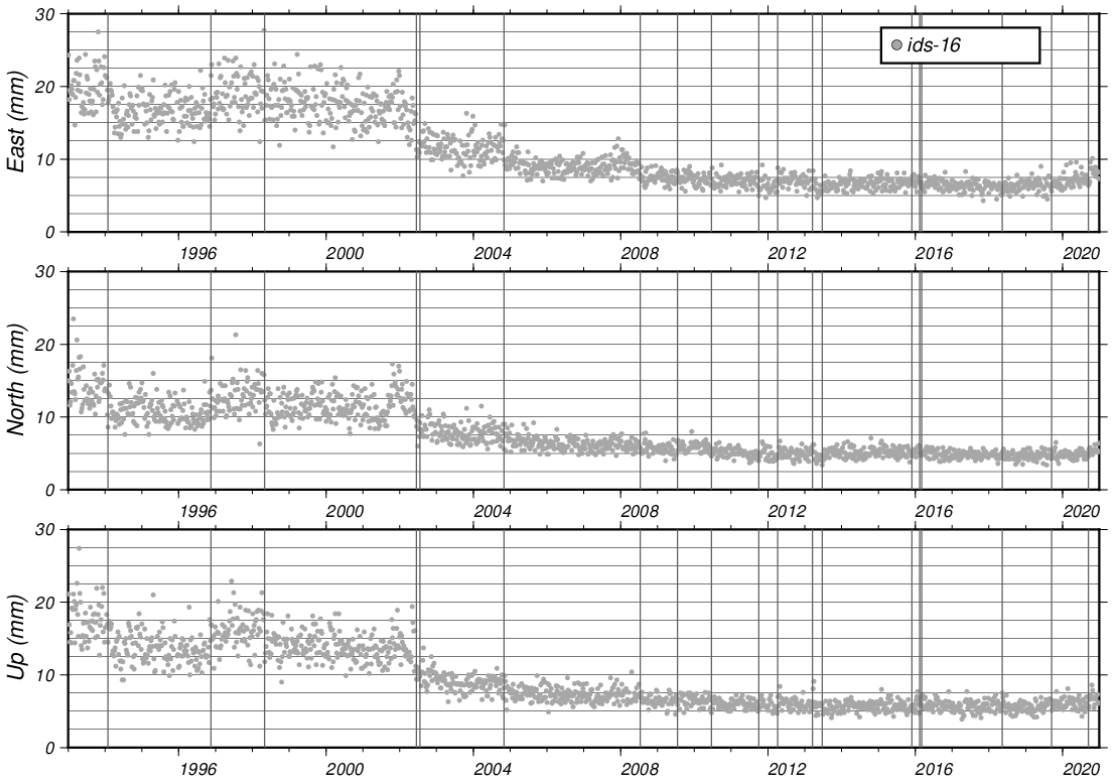

Figure 20: Internal station position residuals of the IDS 16 series (IDS contribution to the ITRF2020).

Table 1: Summary of IDS Analysis Centers.

Analysis Center	Code	Contact(s)
ESA/ESOC, Germany European Space Agency/ Europen Space Operations Center	ESA	Michiel Otten
Geodetic Observatory Pecný, Czech Republic	GOP	Petr Štěpánek
CNES/CLS, France Centre National d'Etudes Spatiales/ Collecte Localisation Satellites	GRG	Hugues Capdeville Jean-Michel Lemoine
NASA/GSFC, USA Goddard Space Flight Center	GSC	Frank G. Lemoine

Table 2: IDS Analysis Center submission summary using Normal Equations(NEQ) or variance-covariance output(COV).

Analysis Center	Software	Sol. Nb.	Sol. Type	Nb. of files	Nb. of sites (stations)	EOPs
ESA	NAPEOS	12/13	NEQ	1447	87 (199)	Motion+rate+LOD
GOP	BERNESE	67	COV	1456	85 (196)	Motion+rate
GRG	GINS/DYNAMO	43	COV	1461	86 (199)	Motion
GSC	GEODYN	51	NEQ	1457	88 (200)	Motion
IDS	CATREF	16	COV	1456	87 (201)	Motion

Table 3: DORIS constellation by IDS Analysis Center.

DORIS Mission	DORIS Receiver	Altitude / Inclination	ESA wd12/13	GOP wd67	GRG wd43	GSC wd51
SPOT-2	1G (1 channel)	802-831 km 98.7°	1993:003 2009:193	1993:003 2009:193	1993:003 2007:308	1993:003 2009:193
TOPEX/ Poseidon	1G (1 channel)	1322-1341 km 66.5°	1993:003 2004:305	1993:003 2004:305	1993:003 2004:298	1993:003 2004:305
SPOT-3	1G (1 channel)	819-846 km 98.6°	1994:030 1996:315	1994:030 1996:315	1994:030 1996:315	1994:037 1996:315
SPOT-4	1G (1 channel)	791-811 km 98.8°	1998:123 2013:174	1998:130 2013:174	1998:123 2012:365	1998:123 2013:013
Envisat	2G (2 channels)	785-791 km 98.6°	2002:167 2012:099	2002:104 2012:099	2005:100 2012:092	2004:305 2012:085
SPOT-5	2GM (2 channels)	825-826 km 98.8°	2002:167 2015:333	2002:167 2015:333	2002:167 2015:326	2002:167 2015:326
Jason-1	2GM (2 channels)	1328-1340 km 66.0°	2002:015 2008:195	Not included	2004:305 2008:188	2004:312 2008:188
Jason-2	DGXX (7 channels)	1328-1340 km 66.0°	2008:195 2018:359	2008:230 2019:251	2008:195 2019:251	2008:195 2019:251
Cryosat-2	DGXX (7 channels)	707-727 km 92.0°	2010:150 -	2010:150 -	2010:171 -	2010:157 -
HY-2A	DGXX (7 channels)	963-963 km 99.4°	2011:275 -	2011:268 2020:250	2011:275 2020:250	2010:311 2020:250
Saral	DGXX (7 channels)	706-772 km 98.65°	2014:001 -	2013:069 -	2013:076 -	2013:076 -
Jason-3	DGXXs (7 channels)	1328-1340 km 66.04°	2016:052 -	2016:045 -	2016:045 -	2016:066 -
Sentinel-3A	DGXXs (7 channels)	802-807 km 98.65°	2016:073 -	2016:073 -	2016:066 -	2016:066 -
Sentinel-3B	DGXXs (7 channels)	802-807 km 98.65°	2018:126 -	2018:154 -	2018:133 -	Not included

Table 4: IDS Analysis Center contribution to the IDS 16 Combined Solution.

IDS Series	Analysis Center	Sol. Nb.	Number of Files	Sites	Stations	Contribution to the Origin	Scale	EOPs
IDS 16	ESA	12/13	1434	83	194	Yes	Yes	No
	GOP	67	1448	83	192	Yes	Yes	Yes
	GRG	43	1457	85	198	Yes	Partially*	Yes
	GSC	51	1453	86	197	Yes	Partially*	Yes

*not between end of TOPEX/Poseidon and start of HY-2A, i.e. 2004:312 and 2011:268

Table 5: Main statistics of thescale and geocenter from IDS 09 (ITRF2014) and IDS 16 (ITRF2020) series wrt ITRF2014. Units are mm.

Series	Time	*Scale*		T_x		T_y		T_z	
Id.	Span	mean	std	mean	std	mean	std	mean	std
IDS 09	1993.0-2002.4	7.47	3.70	-1.48	5.17	-2.51	5.99	-3.70	22.36
IDS 09	2002.4-2008.5	8.89	2.00	-0.97	3.65	1.28	4.27	-17.91	12.71
IDS 09	2008.5-2015.0	7.44	3.50	-2.45	3.27	-0.73	3.60	-8.40	9.27
IDS 16	1993.0-2002.4	13.16	4.27	-0.50	4.64	-3.40	4.92	2.35	22.66
IDS 16	2002.4-2008.5	9.93	1.82	-1.60	3.03	0.11	3.83	-16.01	14.22
IDS 16	2008.5-2015.0	8.98	1.69	-2.62	2.37	1.45	2.25	-8.76	8.20
IDS 16	2015.0-2021.0	10.60	1.64	-3.85	2.09	6.39	2.89	-1.75	10.31

Table 6: Main statistics of WRMS of the station residuals from IDS 09 (ITRF2014) and IDS 16 (ITRF2020) series wrt ITRF2014. Units are mm.

Series	Time	East		North		Up		3D	
Id.	Span	mean	std	mean	std	mean	std	mean	std
IDS 09	1993.0-2002.4	20.43	3.59	13.68	2.67	17.18	3.32	16.76	2.72
IDS 09	2002.4-2008.5	10.19	1.84	7.80	1.24	8.77	1.48	8.79	1.26
IDS 09	2008.5-2015.0	7.72	1.00	6.49	0.96	7.31	1.01	7.13	0.74
IDS 16	1993.0-2002.4	19.90	3.32	12.66	2.37	16.54	3.05	15.89	2.42
IDS 16	2002.4-2008.5	10.43	1.91	7.24	1.15	8.62	1.53	8.52	1.24
IDS 16	2008.5-2015.0	7.59	0.92	6.27	0.77	7.21	0.86	6.90	0.61
IDS 16	2015.0-2021.0	11.31	1.90	8.22	1.09	10.38	1.82	9.63	1.28

Table 7: Main statistics of polar motions from IDS 09 (ITRF2014) and IDS 16 (ITRF2020) series: differences wrt IERS C04 series and formal errors. Units are μas.

Series	Time	Differences wrt IERS C04				Formal errors			
Id.	Span	X-pole		Y-pole		X-pole		Y-pole	
		mean	std	mean	std	mean	std	mean	std
IDS 09	1993.0-2002.4	-26.07	669.15	20.47	625.23	255.24	63.17	252.11	63.06
IDS 09	2002.4-2008.5	73.60	318.90	-48.69	296.26	160.64	31.64	157.73	27.40
IDS 09	2008.5-2015.0	-46.06	245.26	42.06	223.09	148.08	22.74	147.41	24.28
IDS 16	1993.0-2002.4	-37.73	664.02	-10.59	587.73	192.33	77.48	197.20	84.40
IDS 16	2002.4-2008.5	13.84	331.18	38.15	321.24	140.03	29.70	145.87	30.49
IDS 16	2008.5-2015.0	-10.73	208.30	-6.12	193.26	107.24	16.34	107.01	16.39
IDS 16	2015.0-2021.0	18.88	192.05	5.38	171.69	105.40	16.58	102.06	16.13

Table 8: Station discontinuities.

IDS Station	IERS DOMES Number	DORIS Site name	Discontinuity Epoch	Discontinuity Origin
ADEA	91501S001	Terre Adelie	1998/03/25	Earthquake M8.1 Balleny Islands (616km)
ADGB	91501S004	Terre Adelie	2014/06/10	Beacon change
AMTB	91401S003	Amsterdam	2005/11/24	Antenna offset
AMVB	91401S005	Amsterdam	2015/12/14	Beacon change
AMVB	91401S005	Amsterdam	2020/04/12	Earthquake M6.1 Mid-Indian Ridge (95km)
AREA	42202S005	Arequipa	1994/06/09	Earthquake M8.2 La Paz Bolivia (515km)
AREA	42202S005	Arequipa	1996/11/12	Earthquake M7.7 near the coast of central Peru (477km)
AREA	42202S005	Arequipa	2001/06/23	Earthquake M8.4 near the coast of southern Peru (231km)
AREB	42202S006	Arequipa	2002/07/17	Unknown in East and Up
ARFB	42202S007	Arequipa	2008/07/08	Earthquake M6.2 southern Peru (60km)
ARFB	42202S007	Arequipa	2010/05/06	Earthquake M6.2 near the coast of Tarapaca Chile (204km)
ARFB	42202S007	Arequipa	2012/06/07	Earthquake M6.1 southern Peru (118km)
ARFB	42202S007	Arequipa	2016/12/01	Earthquake M6.2 NE of Huarichancara Peru (147km)
ARFB	42202S007	Arequipa	2020/09/09	Unknown in East
ASDB	30602S004	Ascension	2001/03/07	Earthquake M6.0 Ascension Island region (199km)
ASDB	30602S004	Ascension	2003/03/15	New antenna
ASEB	30602S005	Ascension	2015/11/19	Earthquake M5.2 ENE of Georgetown St-Helena (91km)
ASEB	30602S005	Ascension	2016/06/10	Earthquake M5.5 ENE of Georgetown St-Helena (96km)
ASEB	30602S005	Ascension	2017/07/10	Earthquake M5.2 ENE of Georgetown St-Helena (85km)
CADB	41609S002	Cachoeira	2006/01/20	Unknown in Up
CADB	41609S002	Cachoeira	2008/08/02	Unknown in East and Up
CADB	41609S002	Cachoeira	2011/12/21	Unknown in Up
CADB	41609S002	Cachoeira	2016/01/01	Unknown in Up
CHAB	50207S001	Chatham Island	2006/12/06	Antenna problem
CICB	23101S002	Cibinong	2002/10/17	Unknown in North and Up
CICB	23101S002	Cibinong	2006/07/17	Earthquake M7.7 south of Java (317km)
CIDB	23101S003	Cibinong	2009/09/02	Earthquake M7.0 Java (152km)
CIDB	23101S003	Cibinong	2017/12/15	Earthquake M6.5 SSW Kawalu Indonesia (184km)
COBB	49804S004	Cold Bay	2020/07/22	Earthquake M7.8 SSE Perryville Alaska (262km)
COBB	49804S004	Cold Bay	2020/10/19	Earthquake M7.6 SE Sand Point Alaska (208km)
COLA	23501S001	Colombo	1994/11/14	Earthquake M7.1 Mindoro Philippines (4558km)
DIOB	12602S012	Dionysos	2008/01/06	Earthquake M6.2 Southern Greece (145km)
DIOB	12602S012	Dionysos	2008/01/06	Earthquake M6.4 Southern Greece (212km)
EASB	41703S009	Easter Island	2007/03/04	Beacon change
EASB	41703S009	Easter Island	2009/09/17	Earthquake M6.2 Easter Island region (360km)
EASB	41703S009	Easter Island	2011/03/01	Earthquake M6.0 Easter Island region (383km)
EASB	41703S009	Easter Island	2012/05/10	Earthquake M5.9 Easter Island region (362km)
EASB	41703S009	Easter Island	2013/11/02	Earthquake M6.0 Easter Island region (506km)
EVEB	21501S001	Everest	2002/03/16	Unknown in Up
EVEB	21501S001	Everest	2011/09/18	Earthquake M6.9 Sikkim India (134km)
EVEB	21501S001	Everest	2015/04/25	Earthquake M7.8 east of Khudi Nepal (207km)
EVEB	21501S001	Everest	2015/07/04	Post seismic
FAIB	40408S005	Fairbanks	2002/11/03	Earthquake M7.9 Alaska (162km)
FAIB	40408S005	Fairbanks	2003/08/03	Post seismic
FAIB	40408S005	Fairbanks	2006/01/01	Post seismic
GOMB	40405S037	Goldstone	1999/10/16	Earthquake M7.1 southwest of Ludlow CA (86km)
GONC	40405S043	Goldstone	2019/07/06	Earthquake M7.1 Ridgecrest EQ Sequence (93km)
HBMB	30302S008	Hartebeesthoek	2016/09/09	USO change
HELB	30606S003	St-Helena	2000/01/31	Antenna tilt
HEMB	30606S004	St-Helena	2008/08/02	Unknown in Up
HEMB	30606S004	St-Helena	2011/12/19	Beacon change
KESB	91201S004	Kerguelen	2004/02/09	Data gap
KIUB	12334S006	Kitab	2013/05/26	Earthquake M5.7 NNE of Bulung'ur Uzbekistan (99km)
KRAB	12349S001	Krasnoyarsk	1998/09/03	Unknown in East
KRAB	12349S001	Krasnoyarsk	2003/09/27	Earthquake M7.3 southwestern Siberia Russia (740km)
KRUB	97301S004	Kourou	1997/01/02	Unknown in North
KRVB	97301S004	Kourou	2007/10/31	Unknown in East
KRWB	97301S006	Kourou	2015/11/22	Unknown in East

To be continued...

IDS Station	IERS DOMES Number	DORIS Site name	Discontinuity Epoch	Discontinuity Origin
				To continue...
LICB	32809S004	Libreville	2008/08/02	Unknown in Up
LICB	32809S004	Libreville	2011/12/21	Unknown in Up
MAHB	39801S005	Mahe	2009/03/30	Beacon change
MANB	22006S002	Manila	2004/07/10	Data gap
MANB	22006S002	Manila	2010/01/27	Earthquake M5.9 Philippine Islands region (491km)
MANB	22006S002	Manila	2012/06/16	Earthquake M5.9 Luzon Philippines (197km)
MARB	30313S002	Marion Island	2003/01/27	Earthquake M6.4 Prince Edward Islands region (234km)
MATB	30313S003	Marion Island	2006/11/07	Antenna offset
MATB	30313S003	Marion Island	2009/06/04	Earthquake M6.0 Prince Edward Islands region (239km)
MORB	51001S002	Port Moresby	2008/08/30	Earthquake M6.4 eastern New Guinea region (366km)
NOXB	92701S004	Noumea	2014/05/01	Earthquake M6.6 ile Hunter New Caledonia (409km)
NOXB	92701S004	Noumea	2017/11/19	Earthquake M7.0 ENE of Tadine New Caledonia (247km)
PDMB	31906S002	Ponta Delgada	2009/06/03	USO change
RAQB	92403S001	Rapa	1999/09/08	Data gap
REUB	97401S002	La Reunion	2002/01/09	Unknown in Up
REYB	10202S002	Reykjavik	2000/06/17	Earthquake M6.5 Iceland (76km)
REZB	10202S003	Reykjavik	2005/03/14	Unknown in East and North
REZB	10202S003	Reykjavik	2008/05/29	Earthquake M6.3 Iceland (46km)
REZB	10202S003	Reykjavik	2012/05/29	Beacon change
RIOB	41507S004	Rio Grande	1998/06/29	Unknown in North and Up
RIRB	41507S007	Rio Grande	2015/12/09	Unknown in North
ROTA	66007S001	Rothera	2002/01/13	Unknown
SAKA	12329S001	Yuzhno-Sakhalinsk	1994/10/09	Earthquake M7.3 Kuril Islands (534km)
SAKA	12329S001	Yuzhno-Sakhalinsk	1998/12/26	Unknown in East and North
SAKA	12329S001	Yuzhno-Sakhalinsk	2003/09/25	Earthquake M8.2 Hokkaido Japan (588km)
SALB	39601S002	Sal	2008/07/06	Unknown in North
SANA	41705S007	Santiago	1996/03/27	Unknown in North
SANB	41705S009	Santiago	2003/06/20	Earthquake M6.8 Coquimbo Chile (297km)
SANB	41705S009	Santiago	2006/01/01	Unknown in East
SANB	41705S009	Santiago	2008/03/13	Unknown in North and Up
SANB	41705S009	Santiago	2008/12/18	Earthquake M6.2 offshore Valparaiso Chile (125km)
SANB	41705S009	Santiago	2009/05/27	Post-seismic
SANB	41705S009	Santiago	2010/02/27	Earthquake M8.8 offshore Bio-Bio Chile (389km)
SODA	40503S003	Socorro Island	1995/12/26	Volcanic activity
SODA	40503S003	Socorro Island	1997/05/29	Volcanic-activity
SODB	40503S004	Socorro Island	2002/10/03	Earthquake M6.5 gulf of California (569km)
SOEB	40503S005	Socorro Island	2014/11/05	Post-seismic
SPJB	10317S005	Ny-Alesund	2005/04/02	Earthquake M6.1 Svalbard (131km)
SPJB	10317S005	Ny-Alesund	2008/02/21	Earthquake M6.1 Svalbard (256km)
SPJB	10317S005	Ny-Alesund	2009/03/06	Earthquake M6.5 Svalbard (316km)
SPJB	10317S005	Ny-Alesund	2014/02/23	Unknown in Up
SYPB	66006S003	Syowa	2008/07/12	Unknown in East and North
SYPB	66006S003	Syowa	2012/07/11	RF connection problem
THUB	43001S005	Thule	2006/05/30	Ice melting
TLSB	10003S005	Toulouse	2012/10/27	Unknown in Up
TRIA	30604S001	Tristan Da Cunha	1999/07/17	Unknown in Up
TRIB	30604S002	Tristan Da Cunha	2004/07/29	Earthquake M4.5 Tristan da Cunha region (28km)
TRIB	30604S002	Tristan Da Cunha	2009/08/18	Unknown in Up
TRJB	30604S003	Tristan Da Cunha	2016/05/18	Unknown in North and Up

Table 9: Main statistics of WRMS of the station residuals from IDS 16 (ITRF2020) series wrt its cumulative solution. Units are mm.

Series	Time	East		North		Up	
Id.	Span	mean	std	mean	std	mean	std
IDS 16	1993.0-2002.4	17.76	2.61	11.80	2.18	14.56	2.50
IDS 16	2002.4-2008.5	10.06	1.79	6.94	1.28	8.01	1.36
IDS 16	2008.5-2015.0	6.93	0.87	5.22	0.76	6.02	0.78
IDS 16	2015.0-2021.0	6.63	0.88	4.90	0.58	5.83	0.79

Table 10: Main statistics of the 3D tie residuals between the IDS 16 cumulative solution and the DORIS-to-DORIS surveyed ties. Units are *mm*.

Number of ties	Number of sites	Max	Median	Mean	Std	RMS
99	53	58.19	12.69	16.67	10.59	19.72

Appendix A. IDS ACs Standards

Table A.11: Main standards of IDS ACs contributions to the IDS 16 combined solution.

IDS AC	ESA	GOP	GRG	GSC
Series Nb.	wd12/13	wd67	wd43	wd51
Arc length	1 day	1 day	3.5 days	3.5 & 7 days
Station constraints	N/A	10 m	10 m	N/A
EOPs contraints	N/A	500 mas	15 m	N/A
Reference System				
Earth Ref.	DPOD2014v4	DPOD2014v51	DPOD2014v51	DPOD2014v4
Cel. Ref.	inertial J2000	inertial J2000	inertial J2000	inertial J2000
Polar motion	IERS Bull. A	IERS 08 C04	IERS 14 C04	IERS 14 C04
C21, S21	IERS 2010[1]	IERS 2010[1]	IERS 2010[1]	IERS 2010[1]
Pole model	IERS 2010	IERS 2010	IERS 2017	IERS 2017
Prec./Nut.	IERS 2010	IERS 2003	IERS 2010	IERS 2003
Station Displacement				
Solid Earth tides	IERS 2010	IERS 2010	IERS 2010	IERS 2010
Ocean loading	EOT11a	FES2014[2]	FES2014	GOT 4.10c[3]
Tidal atmos. loading	N/A	S1/S2	S1/S2[4]	N/A
Non tidal atmos. load.	N/A	N/A	N/A	N/A
Solid pole tide	IERS 2010	IERS 2010	IERS 2010	IERS 2010
Ocean pole tide	N/A	N/A	N/A	N/A
Tidal geocenter	N/A	N/A	N/A	GOT 4.10c
Gravity				
Gravity field	EIGEN-GRGS RL04 (120)	EIGEN-GL04S$^{<2002.0}$	EIGEN-GRGS.RL04 (95)	GOCO5s[5] (150)
Static		EIGEN-6S2 $^{\geq 2002.0}$		
Gravity field	Up to deg 90	Up to deg 100	Up to deg 50	Up to deg 100
Time variable				[6,7]
Solid Earth tides	IERS 2010	IERS 2010	IERS 2010	IERS 2010
Ocean tides	EOT11a	FES2014	FES2014	GOT 4.10c
Atmos. gravity	AOD1B RL06 (3-hr)[8]	AOD1B RL06 (3-hr)	AOD1B RL06 (3-hr)	AOD1B RL06 (3-hr)
	Up to deg 90	Up to deg 20	Up to deg 50	(for GRACE-FO)
				Up to deg 90
Air tides			AOD1B RL06	AOD1B RL06
Earth pole tide	IERS 2010	IERS 2010	IERS 2017[9]	IERS 2017[9]
Ocean pole tide	IERS 2010	IERS 2010	Desai (2002)	Desai (2002)
			Up to deg 50	Up to deg 60
Third bodies	DE405 (JPL)	DE405 (JPL)	DE421 (JPL)	DE421 (JPL)
DORIS Data				
Troposphere model	Saastamoinen[10]	Saastamoinen		Saastamoinen
Tropo. Mapping Funct.	GMF	GMF	VMF-1	VMF-1
Meteorological Data	GPT	GPT	GPT2	GPT
Tropo. gradients	Yes[11]	No	Yes[11]	No
2nd Order Ionosphere	N/A	N/A	N/A	N/A
Elevation Cut-off	7 deg	10 deg	10 deg	7 deg
Elevation Down-weighting	$1/sin$	$1/sin^2$	$1/sin^2$	$1/sin^{1/2}$

[1] Equation 6.5 of Petit and Luzum (2011)
[2] Lyard et al. (2021)
[3] Ray (2013)
[4] Ray & Ponte (2003)
[5] Mayer-Gürr et al. (2015)
[6] Secular terms from GOCO05s after 2003.0
[7] Annual terms from GOCO05s
[8] Dobslaw et al. (2017)
[9] Linear mean pole adopted in 2017 by the IERS ((Ries et al., 2015);(Ries and Desai, 2017))
[10] Sastamoinen (1972)
[11] Estimate north and east troposphere gradient daily per station.

Appendix B. From NEQ to COV format

So far, the IDS ACs deliver their weekly SINEX solutions with either COV or NEQ content. While a COV SINEX file contains the solution vector (weekly positions and daily EOPs) $\boldsymbol{x}$ and the corresponding aposteriori variance-covariance matrix $\boldsymbol{K}$, a NEQ files include the solution apriori $\boldsymbol{x}_0$, the normal equation matrix $\boldsymbol{N}$ and the normal equation vector $\boldsymbol{b}$. However, almost all the CATREF routines are designed for SINEX files with COV content. Therefore, for solutions in NEQ SINEX format, we first need to convert it in COV format by computing

$$\begin{aligned} \boldsymbol{K} &= \boldsymbol{N}^{-1}, \\ \boldsymbol{x} &= \boldsymbol{x}_0 + \boldsymbol{K}\boldsymbol{b}. \end{aligned}$$

Even if the normal matrix $\boldsymbol{N}$ is theoretically invertible (as any symmetric positive definite matrix), the matrix may be not numerically invertible. To overcome that numerical problem, we add positive elements to the diagonal of the normal matrix so,

$$\boldsymbol{K} \equiv (\boldsymbol{N} + \boldsymbol{\lambda}\boldsymbol{I})^{-1},$$

where $\boldsymbol{I}$ denotes the identity matrix. To define the regularization vector $\boldsymbol{\lambda}$, the IDS CC took benefit of some weeks for which the normal matrix $\boldsymbol{N}$ was numerically invertible to test several values. The tests included analysis of the impact on the solution vector $\boldsymbol{x}$. Then, for the ITRF2020 processing, the regularization vector $\boldsymbol{\lambda}$ was set with one values for the station positions and zero values elsewhere.

Appendix C. Combination Model

The IDS combination problem consists in estimating

- weekly positons X_c^i of a set of $i = \{1, \cdots, m\}$ stations
- daily x- and y-pole coordinates $\left(xp_c^j, yp_c^j\right)_{j=1,\cdots,7}$

expressed in the c combined reference frame from

- weekly station positions X_s^i
- daily pole coordinates (xp_s, yp_s)

associated to $s = 1, \cdots, n$ AC individual solutions expressed in n individual reference frames. Then, for each AC individual solution s, the combination

equations read as:

$$\begin{cases} X_s^1 &= T_s + (1+\alpha_s)\, X_c^1 + \mathcal{R}_s\, X_c^1 \\ \vdots & \vdots & \vdots \\ X_s^m &= T_s + (1+\alpha_s)\, X_c^m + \mathcal{R}_s\, X_c^m \\ xp_s^1 &= xp_c^1 + \theta_s^y \\ \vdots & \vdots & \vdots \\ xp_s^7 &= xp_c^7 + \theta_s^y \\ yp_s^1 &= yp_c^1 + \theta_s^x \\ \vdots & \vdots & \vdots \\ yp_s^7 &= yp_c^7 + \theta_s^x \end{cases} \tag{C.1}$$

where α_s, $T_s = (T_s^x, T_s^y, T_s^z)^T$ and $\mathcal{R}_s$ denotes, respectively, the scale factor, the translation vector and the rotation matrix from the c to the s reference frame. Furthermore, the rotation matrix can be expressed in terms of the rotation angles $\theta_s^{x,y,z}$ with:

$$\mathcal{R}_s = \begin{bmatrix} 0 & -\theta_s^z & \theta_s^y \\ \theta_s^z & 0 & -\theta_s^x \\ -\theta_s^y & \theta_s^x & 0 \end{bmatrix}. \tag{C.2}$$

If we linearize the unknowns (i.e. station positions and EOPs in the *cc* combined frame as well as the seven transformation parameters) around their approximate/apriori values, Eqs. C.1 can be rewritten by mean of the following linear system:

$$\underbrace{\begin{bmatrix} \boldsymbol{I}_{3m+14} & \boldsymbol{A1}_s \\ & \boldsymbol{A2}_s \end{bmatrix}}_{\boldsymbol{A}_s} \cdot \underbrace{\begin{bmatrix} \delta\Lambda_c \\ \delta\Gamma_s \end{bmatrix}}_{\boldsymbol{\chi}_s} = \mathbf{b}_s, \tag{C.3}$$

where $\delta\Lambda_c$ is the vector of unknown station positions and EOPs, $\delta\Gamma_s$ is the vector of unknown transformation parameters (between c and s reference frames), i.e.

$$\delta\Lambda_c^T = \left(\left(\delta x_c^i, \delta y_c^i, \delta z_c^i\right)_{i=1}^m, \delta xp_c^{i=1,\cdots,7}, \delta yp_c^{i=1,\cdots,7} \right),$$

$$\delta\Gamma_s^T = \left(\delta T_s^x, \delta T_s^y, \delta T_s^z, \delta\alpha_s, \delta\theta_s^x, \delta\theta_s^y, \delta\theta_s^z\right),$$

where $\boldsymbol{I}_k$ denotes the k-by-k identity matrix and with

$$\boldsymbol{A1}_s = \begin{bmatrix} 1 & 0 & 0 & x_0^1 & 0 & z_0^1 & -y_0^1 \\ 0 & 1 & 0 & y_0^1 & -z_0^1 & 0 & x_0^1 \\ 0 & 0 & 1 & z_0^1 & y_0^1 & -x_0^1 & 0 \\ \vdots & \vdots & \vdots & \vdots & \vdots & \vdots & \vdots \\ 1 & 0 & 0 & x_0^m & 0 & z_0^m & -y_0^m \\ 0 & 1 & 0 & y_0^m & -z_0^1 & 0 & x_0^m \\ 0 & 0 & 1 & z_0^m & y_0^1 & -x_0^m & 0 \end{bmatrix}, \quad \boldsymbol{A2}_s = \begin{bmatrix} 0 & 0 & 0 & 0 & 0 & 1 & 0 \\ \vdots & \vdots & \vdots & \vdots & \vdots & \vdots & \vdots \\ 0 & 0 & 0 & 0 & 0 & 1 & 0 \\ 0 & 0 & 0 & 0 & 1 & 0 & 0 \\ \vdots & \vdots & \vdots & \vdots & \vdots & \vdots & \vdots \\ 0 & 0 & 0 & 0 & 1 & 0 & 0 \end{bmatrix}. \tag{C.4}$$

Then, least-squares adjustment yields solution $\widehat{\boldsymbol{\chi}_s}$ of Eq. C.3 as follows:

$$\widehat{\boldsymbol{\chi}_s} = \left(\boldsymbol{A}_s^T\, \boldsymbol{W}_s\, \boldsymbol{A}_s\right)^{-1}\, \boldsymbol{A}_s^T\, \boldsymbol{W}_s\, \mathbf{b}_s,$$

where $\boldsymbol{W}_s$ denotes the weighting matrix. For the whole combination (with the n individual solutions s), the weighting matrix is block diagonal with block s set as the scaled inverse of the variance-covariance matrix $\mathbf{C}_s$ of the solution s, i.e. $\boldsymbol{W}_s = \sigma_s^2\, \mathbf{C}_s^{-1}$. If we denote by $\boldsymbol{\nu}_s$ the vector of the station position posfit residuals of the solution s, the variance factor is computed by:

$$\sigma_s^2 = \frac{\boldsymbol{\nu}_s^T\, \mathbf{C}_s^{-1}\, \boldsymbol{\nu}_s}{f_s}$$

with

$$f_s = 3m - tr\left(\widetilde{\boldsymbol{A}}_s\, \boldsymbol{\Pi}\, \widetilde{\boldsymbol{A}}_s^T\, \mathbf{C}_s^{-1}\right),$$

where $\boldsymbol{\Pi}$ is the inverse of the normal matrix associated with the whole combined linear system (including all the individual AC solutions) and $\widetilde{\boldsymbol{A}}_s$ is the design matrix of partial derivatives of solution s (extension of matrix $\boldsymbol{A}_s$ of Eq. C.3 to the whole combined linear system). To prevent from the rank deficiency of the whole combined normal system and to avoid the remedy to any external frame, we add so-called internal constraints of the seven transformation parameters. Each week and for each transformation parameter P, the internal constraint reads as:

$$\sum_{s=1}^{p} P_s = 0 \qquad (p \leq n).$$

Excluding one individual solution from the above equation implies that the corresponding solution parameter does not contribute to the combined parameter.

Appendix D. Stacking Model

The estimation of the IDS cumulative position and velocity solution from the IDS 16 combined series consists in computing mean positions X_c^i (at epoch t_c) and velocities $\dot{X}_c^i$ of $i = 1, \cdots, m$ stations from weekly positions X_j^i (at epoch t_j) using the following equation

$$X_j^i = T_j + (1 + \alpha_j)\; X_c^i + \mathcal{R}_j\, X_c^i + (t_j - t_c)\; \dot{X}_c^i, \tag{D.1}$$

where α_j, $T_j = \left(T_j^x, T_j^y, T_j^z\right)^T$ and $\mathcal{R}_j$ denotes the scale factor, the translation vector and the rotation matrix (similar to Eq. C.2) from the the long term to the weekly reference frame. After linearizaton of the unknowns around their approximate/apriori values, Eqs. D.1 can be rewritten with:

$$\left[\; \boldsymbol{A3}_j \quad \boldsymbol{A1}_j \;\right] \cdot \left[\; \begin{array}{c} \delta X \\ \delta \Gamma_j \end{array} \;\right] = \mathbf{d}_j, \tag{D.2}$$

where δX is the vector of unknown station positions and velocities, $\delta\Gamma_j$ is the vector of unknown transformation parameters for week j, i.e.

$$\delta X^T = \left(\left(\delta x_c^i, \delta y_c^i, \delta z_c^i, \delta \dot{x}_c^i, \delta \dot{y}_c^i, \delta \dot{z}_c^i \right)_{i=1}^m \right),$$

$$\delta \Gamma_j^T = \left(\delta T_j^x, \delta T_j^y, \delta T_j^z, \delta \alpha_j, \delta \theta_j^x, \delta \theta_j^y, \delta \theta_j^z \right),$$

where the design matrix $\boldsymbol{A1}_j$ is given by Eq. C.4 and with

$$\boldsymbol{A3}_j = \begin{bmatrix} \widetilde{A3}_j & \mathbf{0} & \cdots & \mathbf{0} \\ \mathbf{0} & \widetilde{A3}_j & \ddots & \vdots \\ \vdots & \ddots & \ddots & \mathbf{0} \\ \mathbf{0} & \cdots & \mathbf{0} & \widetilde{A3}_j \end{bmatrix}, \quad \widetilde{A3}_j = \begin{bmatrix} \boldsymbol{I}_3 & (t_j - t_c)\, \boldsymbol{I}_3 \end{bmatrix}.$$

As the combination linear system, the linear problem of Eq. D.2 can be solved by the least-squares method. To overcome the rank deficiency of the whole normal matrix (corresponding to the stacking over n weeks), we add internal constraints on the seven transformation parameters, i.e. adding the conditions for each parameter weekly time series P_k:

$$\begin{cases} \displaystyle\sum_{k=1}^{K} P_k & = & 0 \\ \\ \displaystyle\sum_{k=1}^{K} (t_k - t_c)\ P_k & = & 0 \end{cases} \tag{D.3}$$

where K denotes the total number of stacking weeks (1456 in the case of IDS 16). In the case of stacking, the internal constraints were introduced in CATREF (see Section 4.3 of Altamimi et al., 2007) to preserve the intrinsic physical parameters without involving any external frame.